JGR Oceans

RESEARCH ARTICLE

10.1029/2024JC021518

Genesis and Propagation of Low-Frequency Abyssal *T*-Waves

Zhichao Shen[1], **Wenbo Wu**[1], **and Jörn Callies**[2]

[1]Department of Geology and Geophysics, Woods Hole Oceanographic Institution, Woods Hole, MA, USA, [2]Division of Geological and Planetary Sciences, California Institute of Technology, Pasadena, CA, USA

Key Points:

- Numerical simulations and repeating earthquakes are used to interrogate the genesis and propagation of low-frequency abyssal *T*-waves
- Synthetic abyssal *T*-waves indicate that seafloor scattering contributes significantly more than sea surface roughness and internal waves
- High repeatability of *T*-waves from abyssal repeating earthquakes greatly expands the data spectrum of seismic ocean thermometry

Supporting Information:

Supporting Information may be found in the online version of this article.

Correspondence to:

W. Wu,
wenbo.wu@whoi.edu

Citation:

Shen, Z., Wu, W., & Callies, J. (2024). Genesis and propagation of low-frequency abyssal *T*-waves. *Journal of Geophysical Research: Oceans*, *129*, e2024JC021518. https://doi.org/10.1029/2024JC021518

Received 2 JUL 2024
Accepted 19 SEP 2024

Author Contributions:

Conceptualization: Wenbo Wu
Data curation: Zhichao Shen, Wenbo Wu
Formal analysis: Zhichao Shen, Wenbo Wu, Jörn Callies
Funding acquisition: Wenbo Wu, Jörn Callies
Investigation: Zhichao Shen, Wenbo Wu, Jörn Callies
Methodology: Zhichao Shen, Wenbo Wu, Jörn Callies
Project administration: Wenbo Wu, Jörn Callies
Resources: Wenbo Wu, Jörn Callies
Software: Zhichao Shen, Wenbo Wu, Jörn Callies
Supervision: Wenbo Wu, Jörn Callies
Validation: Zhichao Shen, Wenbo Wu, Jörn Callies
Visualization: Zhichao Shen
Writing – original draft: Zhichao Shen
Writing – review & editing: Zhichao Shen, Wenbo Wu, Jörn Callies

Abstract Abyssal *T*-waves are seismo-acoustic waves originating from abyssal oceans. Unlike subduction-zone-generated slope *T*-waves which are generated through multiple reflections between the sea surface and the gently dipping seafloor, the genesis of abyssal *T*-waves cannot be explained by the same theory. Several hypotheses, including seafloor scattering, sea surface scattering, and internal-wave-induced volumetric scattering, have been proposed to elucidate their genesis and propagation. The elusive mechanism of abyssal *T*-waves, particularly at low-frequencies, hinders their use to quantify ocean temperatures through seismic ocean thermometry (SOT) and estimate oceanic earthquake parameters. Here, using realistic geophysical and oceanographic data, we first conduct numerical simulations to compare synthetic low-frequency abyssal *T*-waves under different hypotheses. Our simulations for the Romanche and Blanco transform faults suggest seafloor scattering as the dominant mechanism, with sea surface and internal waves contributing marginally. Short-scale bathymetry can significantly enhance abyssal *T*-waves across a broad frequency range. Also, observed *T*-waves from repeating earthquakes in the Romanche, Chain, and Blanco transform faults exhibit remarkably high repeatability. Given the dynamic nature of sea surface roughness and internal waves, the highly repeatable *T*-wave arrivals further support the seafloor scattering as the primary mechanism. The dominance of seafloor scattering makes abyssal *T*-waves useable for constraining ocean temperature changes, thereby greatly expanding the data spectrum of SOT. Our observations of repeating abyssal *T*-waves in the Romanche and Chain transform faults could provide a valuable data set for understanding Equatorial Atlantic warming. Still, further investigations incorporating high-resolution bathymetry are warranted to better model abyssal *T*-waves for earthquake parameter estimation.

Plain Language Summary Earthquakes occurring deep beneath the ocean can create underwater sound waves known as abyssal *T*-waves. Unlike the sound waves produced by earthquakes in subduction zones, where an oceanic plate dives beneath a continent, the origin of abyssal *T*-waves is not fully understood. Understanding these waves is crucial, as how fast they travel in the water column could be used to measure ocean temperature changes. Scientists have proposed several hypotheses, like wave scattering from the seafloor, sea surface, or internal waves. In this study, we use numerical modeling and real data from repeating earthquakes to test these hypotheses. Our modeling results suggest that abyssal *T*-waves mostly come from the seafloor scattering, which is further confirmed by the highly repeatable nature of abyssal *T*-waves from repeating earthquakes. We also find that fine-scale seafloor features can significantly amplify these scattered waves. Our results indicate that abyssal *T*-waves from mid-ocean ridges and transform faults could help monitor ocean temperature changes. For example, repeating abyssal *T*-waves in the Chain and Romanche transform faults show potential in understanding the ocean warming in the Equatorial Atlantic. Still, improved bathymetry data are needed to better model and fully harness abyssal *T*-waves.

1. Introduction

Generated from natural earthquakes, *T*-waves are seismo-acoustic waves that propagate horizontally within the ocean's SOund Fixing And Ranging (SOFAR) channel, where sound speed reaches a minimum (Linehan, 1940; Tolstoy & Ewing, 1950). With a speed of ~1.5 km/s, *T*-waves can travel over long distances (up to tens of thousands of kilometers) in the ocean with little energy dissipation, making them widely detectable by hydrophones, ocean bottom seismometers (OBS), and even land stations (Okal, 2008). Due to their ubiquitous presence and efficient long-range transmission, *T*-waves have become a valuable tool for monitoring oceanic seismicity (Fox et al., 2001; Hanson & Bowman, 2006; Parnell-Turner et al., 2022; Smith et al., 2002; Yun et al., 2022) and volcanism (Tepp & Dziak, 2021; Wech et al., 2018), profoundly enhancing our understanding of tectonic and volcanic processes in remote oceans (Dziak et al., 2011, 2012; Norris & Johnson, 1969). *T*-waves can also help constrain ocean temperature changes through seismic ocean thermometry (SOT; Wu et al., 2020). The SOT approach enables the linkage of the travel time variations of low-frequency *T*-waves (<5 Hz) from repeating earthquakes to ocean temperature anomalies. Recent applications of SOT in the equatorial Indian Ocean and the Kuroshio Extension region have highlighted the effects of mesoscale eddies and decadal ocean warming trends with reduced uncertainties (Callies et al., 2023; Peng et al., 2024; Wu et al., 2023).

While *T*-waves have significantly deepened our insights into geophysical and oceanographic processes in recent decades, their genesis and propagation, particularly those originating from deep oceans, remain incompletely understood. In general, *T*-waves can be categorized into two groups: slope *T*-waves and abyssal *T*-waves (de Groot-Hedlin & Orcutt, 2001; Okal, 2008). Slope *T*-waves are primarily generated from shallow subduction zone earthquakes. Their genesis involves a downslope conversion mechanism, where seismic energy can be effectively confined to the SOFAR channel through multiple reflections between the sea surface and the gently sloping seafloor (Chiu, 1994; Johnson et al., 1963). In contrast, abyssal *T*-waves are generated by earthquakes in abyssal plains and exhibit distinct characteristics, including higher frequency content (10–60 Hz), reduced low-frequency (<10 Hz) energy, and a notably symmetric coda surrounding the peak frequency arrival compared to slope *T*-waves (Duennebier, 1968; Johnson et al., 1968; Keenan & Merriam, 1991). However, the term "abyssal *T*-wave" often lacks a definitive water depth range for abyssal plains. Henceforth, we define it as those generated from earthquakes wherein the seafloor lies below the conjugate water depth at which the sound velocity equals that at the sea surface (C. M. Williams et al., 2006). In such a scenario, the seafloor is too deep to geometrically guide seismic waves into the SOFAR channel, requiring a non-geometric scattering mechanism to account for the genesis of abyssal *T*-waves (Okal, 2008).

Several hypotheses have been proposed to explain their genesis and propagation. Even though the early observations of abyssal *T*-waves were documented in the 1960s (Duennebier, 1968; Duennebier & Johnson, 1967; Johnson et al., 1968), the coupling of Stoneley waves with the SOFAR channel proposed by Biot (1952) could result in the development of abyssal *T*-waves. Nonetheless, this theory fails to account for the observed decrease in low-frequency amplitudes (Bottero, 2018; Okal, 2008). After examining the spectra of abyssal *T*-waves, Johnson et al. (1968) later attributed their genesis to non-geometric scattering due to sea surface roughness. Similarly, abyssal *T*-waves in polar regions could be excited by underside scattering of sea ice (Keenan & Merriam, 1991). Recently, Godin (2021) also identified sea surface scattering as a viable explanation for key observations of abyssal *T*-waves, showing comparable excitation efficiency to the downslope conversion mechanism. In addition, seafloor scattering can reproduce observed abyssal *T*-wave envelopes by summing several low order modes excited by point sources distributed over the ocean bottom, making it the most appealing hypothesis (de Groot-Hedlin & Orcutt, 1999, 2001; Park et al., 2001; Yang & Forsyth, 2003). Nonetheless, high-resolution seafloor data with spatial resolution comparable to the wavelengths of abyssal *T*-waves are limited, leaving the quantitative comparison of different scattering mechanisms unexplored. Furthermore, internal-wave-induced sound-speed perturbations contribute the most acoustic scattering at high frequencies (Colosi, 2016; Dushaw et al., 2017). While these volumetric heterogeneities are considered negligible in exciting abyssal *T*-waves (Godin, 2021), their effects can accumulate during the propagation (Colosi et al., 1994; K. L. Williams et al., 2001). For example, the sound speed perturbations due to internal waves along the propagation path can distort the acoustic wavefront, leading to arrival time biases in high-frequency acoustics (Colosi, 2016; Colosi et al., 1994). However, these effects have yet to be quantified for low-frequency abyssal *T*-waves.

The imperfect understanding of the genesis and propagation of abyssal *T*-waves, especially at low frequencies (<5 Hz), could transfer uncertainty into SOT applications and earthquake parameter estimates. First, it remains unclear if low-frequency abyssal *T*-waves can be used to constrain ocean temperature changes, as the repeatability of abyssal *T*-waves would be affected under different genesis hypotheses. For example, seafloor scattering could yield repeatable abyssal *T*-waves from repeaters enabling their use in SOT. In contrast, the temporal variability of sea surface roughness (Semedo et al., 2011) and internal waves (Garrett & Munk, 1972, 1975) can disrupt sea state coherence over the time interval of repeating earthquakes, thus likely producing incoherent *T*-waves not useable for SOT. Second, when determining source parameters (e.g., locations and magnitudes) with *T*-waves, it often assumes a proportional relationship between these parameters and *T*-wave envelope features, such as amplitude and peak energy arrival (Okal, 2008; Olive & Escartín, 2016; Pan & Dziewonski, 2005; Parnell-Turner et al., 2022; Yun et al., 2022). This assumption hinges on the level of seismic-to-acoustic coupling, intricately linked to the generation and propagation mechanism of abyssal *T*-waves, posing challenges in quantifying source

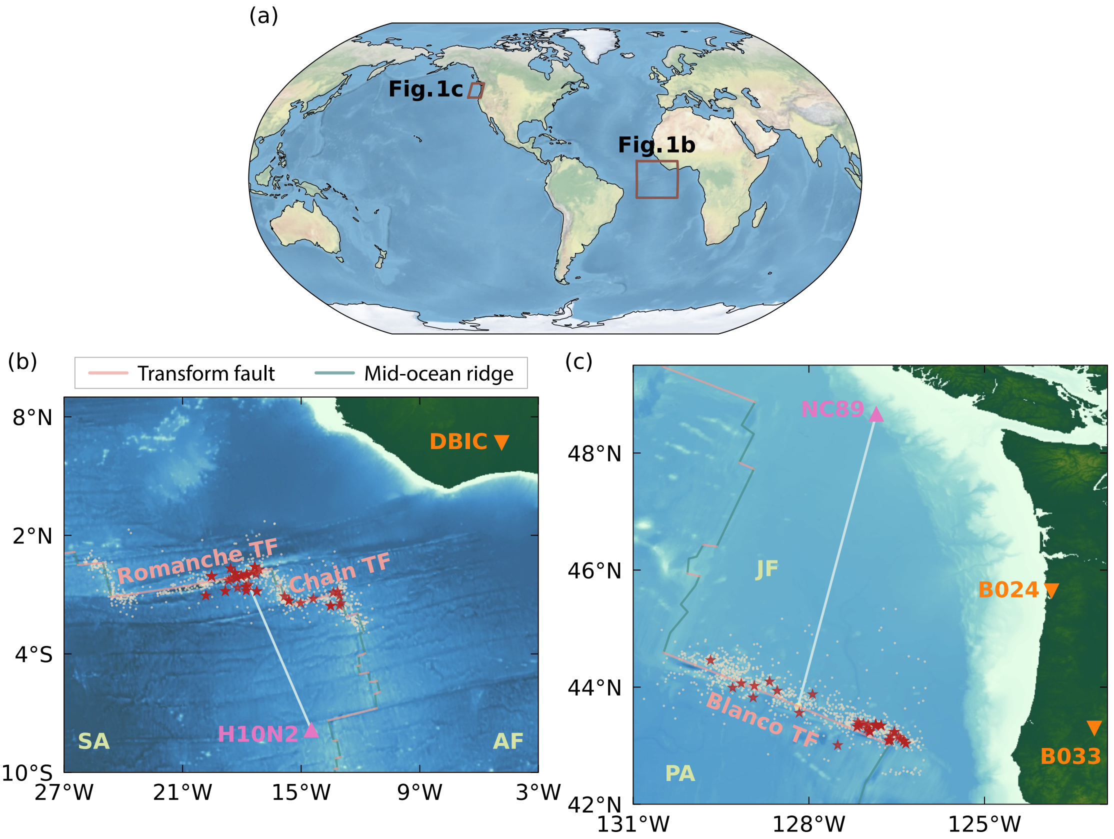

Figure 1. Map view of our study region. (a). Global map showing the Romanche, Chain, and Blanco TFs. (b). Map view of the Romanche and Chain TFs with background seismicity (white dots), *P*-wave station DBIC (orange triangle), and hydrophone H10N2 (pink triangle). The background seismicity is from the global ISC (International Seismological Center) catalog (Bondár & Storchak, 2011). Red stars represent repeating earthquakes. The white line depicts the raypath from the center of background seismicity to H10N2. Green and light-pink lines indicate mid-ocean ridges and transform faults (Bird, 2003), respectively. AF and SA denote the African plate and the South American plate, respectively. (c). Map view of the Blanco TF with background seismicity (white dots), repeating earthquakes (red stars), *P*-wave stations B024 and B032 (orange triangles), and OBS NC89 (pink triangle). PA and JF denote the Pacific plate and the Juan de Fuca plate, respectively.

parameters. For instance, the major arrivals of low-frequency abyssal *T*-waves would more reflect the seismic-acoustic conversion zone, which may not precisely correspond to the earthquake epicenter (Lecoulant et al., 2019; Oliveira & Lin, 2019).

To investigate the genesis and propagation of low-frequency abyssal *T*-waves, we first conduct numerical simulations to compare synthetic *T*-waves generated through seafloor scattering, sea surface scattering and volumetric scattering. Using examples from the Romanche and Blanco transform faults (TF), we describe our model setup of realistic bathymetry, sea surface roughness, and internal-wave-induced sound-speed perturbations in Section 3. Our systematic comparison in Section 4 indicates that seafloor scattering plays a dominant role in the generation and propagation, while sea surface and internal waves contribute marginally. Beyond numerical simulations, we analyze the repeatability of low-frequency abyssal *T*-waves in Section 5, using repeating earthquakes in the Romanche, Chain, and Blanco TFs. The observed high waveform coherence further confirms seafloor scattering as the primary mechanism, enabling the use of SOT with abyssal *T*-waves. Moreover, the effect of seafloor scattering on the seismic applications of abyssal *T*-waves is discussed in Section 6, highlighting the need for more high-resolution bathymetry to better quantify uncertainties of abyssal *T*-wave applications.

2. Data

Located in the Equatorial Atlantic, the Romanche and Chain TFs offset the Mid-Atlantic Ridge by ~950 and ~300 km, respectively (Figure 1b; Bonatti et al., 1994; Harmon et al., 2018; Heezen et al., 1964; Hess, 1955; Sykes, 1967). One reason to select the Romanche and Chain TFs for this study is due to their active seismicity

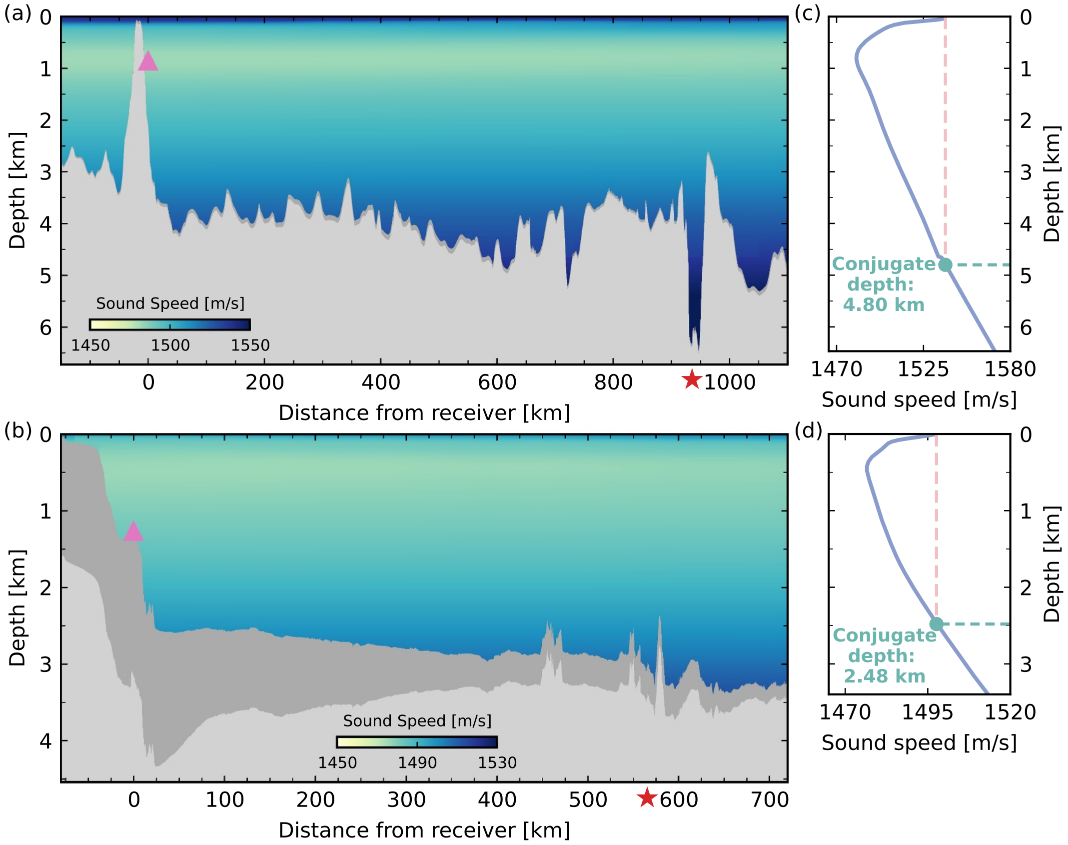

Figure 2. Sound speed, bathymetry and sediment profiles for the Romanche and Blanco TFs. (a). Profile section from the Romanche TF to H10N2. The red star indicates the horizontal location of the source in our numerical simulations, defined as the center of background seismicity. The pink triangle represents the hydrophone location. The dark-gray and light-gray regions denote sediment and underlying bedrock, respectively. (b). Similar to (a), but for the Blanco profile. (c). Averaged 1D sound speed profile for the Romanche TF path shown in (a). (d). Similar to (c), but for the Blanco TF path shown in (b).

(Figure 1b; Bondár & Storchak, 2011). As major tectonic boundaries, the Romanche and Chain TFs can host both local micro-earthquakes (Leptokaropoulos et al., 2023; Schlaphorst et al., 2023; Yu et al., 2021) and strong events with magnitudes reaching up to Mw7 (Abercrombie & Ekström, 2001; Hicks et al., 2020). Apart from the reliable source of seismic events, another reason to select these TFs is the availability of short-distance hydrophone of H10N2 near Ascension Island, operated by the Comprehensive Nuclear-Test-Ban Treaty Organization (CTBTO; Coyne et al., 2012). This short distance reduces the effect of ocean temperature fluctuations on *T*-wave distortion, allowing us to examine the scattering due to sea surface roughness and internal waves by assessing the repeatability of abyssal *T*-waves from repeating earthquakes. To identify repeating earthquakes in this region, we use a land station DBIC, situated in a low-noise environment suitable for regional and teleseismic *P*-wave observations (Figure 1b). For abyssal *T*-waves, we use data from hydrophone H10N2 located ~900 km south of the Romanche and Chain TFs (Figure 1b). H10N2 is deployed at a water depth of 845 m (Figure 2a), ideal for recording high-quality *T*-waves (Wu et al., 2023). The data available for both DBIC and H10N2 spans from 2006 to 2023, providing us an 18-year window to conduct thorough analyses of abyssal *T*-waves.

The Blanco TF in the northeast Pacific, spanning ~350 km, is another important plate boundary, separating the Juan de Fuca plate and the Pacific plate (Figure 1c). It also exhibits abundant seismic activity (Figure 1c; Fox et al., 1994; Kuna et al., 2019; Shen & Wu, 2024). To identify repeating earthquakes along the Blanco TF, we utilize two high-quality regional seismic stations, B024 and B033, offering improved azimuthal coverage compared to the single station DBIC available for the Romanche and Chain TFs (Figures 1b and 1c). For abyssal *T*-wave observations in the Blanco TF, we use an OBS NC89 at a water depth of 1,258 m, from the North-East Time-series Pacific Undersea Networked Experiments (NEPTUNE; Barnes et al., 2008) off the coast of British Columbia (Figure 1c). The NEPTUNE OBS array has demonstrated high sensitivity to abyssal *T*-waves from

Blanco earthquakes (Dziak et al., 2012; Shen & Wu, 2024). The data available for land stations and OBS covers a decade, ranging from 2013 to 2023.

To numerically model low-frequency abyssal *T*-waves, we extract realistic bathymetry profiles from the Global Multi-Resolution Topography (GMRT) synthesis, which integrates ship-based high-resolution multibeam sonar data in some regions (Ryan et al., 2009). For example, the high-resolution multibeam data are collected near the Chain and Blanco TFs (Harmon et al., 2018; Ryan et al., 2009), whereas they are not available for the Romanche TF. In places where high-resolution data are unavailable, the GMRT data are supplemented with bathymetric depths derived from satellite altimetry (Ryan et al., 2009; Sandwell et al., 2021). These interpolated data are essentially equivalent to the General Bathymetric Chart of the Oceans (GEBCO) product with a grid interval of 15 arc-seconds (Tozer et al., 2019). The effects of high-resolution short-scale bathymetry (i.e., wavelengths of <1 km) on the genesis of abyssal *T*-waves will be discussed in Section 4.1. The water depths in the vicinity of the Romanche/Chain and Blanco TFs exceed 6.0 and 3.0 km, respectively (Figure 2). Below the seafloor, we adopt a global 5-arc-minute sediment thickness model GlobSed for Romanche and Blanco profiles (Straume et al., 2019). Due to the limited sediment supply, the Romanche profile exhibits thin sediment along the source-receiver path with an average thickness of 75 m (Figure 2a). While the Blanco profile presents much thicker sediment transported from the North America continent, with an average thickness of 770 m and reaching up to ∼2 km near NC89 (Figure 2b).

Above the seafloor, we use salinity, temperature, and pressure data to compute background ocean density and sound speed profiles. These climatological data are sourced from the Estimating the Circulation and Climate of the Ocean project (ECCO; Forget et al., 2015), spanning from 2006 to 2015. While changes in ocean temperature and salinity can affect *T*-wave arrival times, the focus of this study is to evaluate the proposed different scattering mechanisms. Thus, the 10-year ECCO data provides a sufficiently long period to establish a reference ocean state and sound speed profile for this purpose. To model sea surface roughness, we collect global significant wave height (SWH) and peak period data from the fifth generation of the European Centre for Medium-Range Weather Forecasts Atmosphere Reanalysis of the Global Climate (ERA5; Hersbach et al., 2020), covering the period from 2006 to 2023. The SWH represents the mean wave height of the highest one-third of sea surface waves, while the peak period refers to the period of the most energetic waves. The rich ERA5 data set, with its hourly resolution, allows us to accurately describe the sea state and its effects on low-frequency abyssal *T*-waves.

3. Numerical Model Setup

With realistic geophysical and oceanographic data, we setup two-dimensional (2D) elastic models for wavefield simulations using a Spectral Element Method (SEM) software package SEPCFEM2D (Komatitsch & Tromp, 1999; Komatitsch & Vilotte, 1998). The SEM integrates spectral and finite element approaches, enabling accurate modeling of wave propagation in complex scenarios, including rough interfaces, heterogeneous media, and seismic-acoustic coupling (Bottero et al., 2020; Jamet et al., 2013). Here, we focus on 2D scenarios because of the high computational expense for full three-dimensional simulations. Although 3D effects can affect the excitation and propagation of abyssal *T*-waves (Lecoulant et al., 2019, 2021), our 2D simulations aim to effectively understand and compare the roles of different scattering mechanisms in these processes. The following subsections elaborate our SEM profile setup and stochastic implementation of sea surface and internal-wave-induced sound-speed perturbations.

3.1. SEM Profile

The Romanche and Blanco profiles are sliced from the center of their background seismicity to H10N2 and NC89, respectively (Figures 1 and 2). Specifically, the Romanche profile spans 1,250 km in length and 40 km in depth, whereas the dimension of the Blanco profile is 800 km (horizontal) by 40 km (vertical). Our density and velocity model can be divided into three layers: ocean, sediment, and the underlying solid Earth (Figure 2), similar to Wu et al. (2023). In the ocean layer, we average the ECCO salinity and temperature data and convert them into ocean density and sound speed as the background model (Figure 2) through a Gibbs Seawater Oceanographic Toolbox (McDougall & Barker, 2011). The conjugate water depths in the Romanche and Blanco profiles correspond to 4.80 and 2.48 km, respectively, which is above the local seafloor (Figure 2), meeting our definition of abyssal *T*-waves. The seismic velocity and density in the sediment layer are calculated using empirical functions derived from deep-sea sediments (Hamilton, 1976, 1979). To ensure numerical stability, the *S*-wave velocity at the top of the sediment is constrained to a minimum of 1,500 m/s. For the underlying solid Earth, we adopt uniform velocity and density models with a *P*-wave velocity of 5,800 m/s, a *S*-wave velocity of 3,200 m/s, and a density of 2,600 kg/m^3. To enhance long-duration *T*-waves, we superimpose additional small-scale heterogeneities in this uniform layer, described by an exponential autocorrelation function with an isotropic correlation length of 2 km and root-mean-square perturbation of 3.0% for *P*-wave velocity and density and 4.5% for *S*-wave velocity (Sato et al., 2012).

For each simulation, we use fine-grid meshes of 50 m by 50 m for the ocean and sediment layers, and coarse-grid meshes of 50 m (horizontal) by 250 m (vertical) for the underlying solid Earth. A Heaviside-type explosive source is implemented at a depth of 10 km below the sea surface and a horizontal distance of 935 and 565 km in the Romanche and Blanco profiles, respectively (Figure 2). The source depth of 10 km is chosen as the nominal depth of oceanic earthquakes in the ISC (International Seismological Center; Bondár & Storchak, 2011) catalog. Generally, transform fault earthquakes are thought to occur above the source depth of the 600°C isotherm (Abercrombie & Ekström, 2001; Boettcher et al., 2007), which represents the transition from brittle to ductile deformation. In the Romanche and Blanco TFs, the 600°C isotherm corresponds to depths of 20–25 km (Schlaphorst et al., 2023; Yu et al., 2021) and 10–15 km (Braunmiller & Nábělek, 2008; Kuna et al., 2019; Zang et al., 2024), respectively, justifying our choice of the 10-km source depth. The effect of source depth on the genesis of abyssal *T*-waves will be discussed in Section 4.1. Receivers are placed at 0 km with water depths of 845 and 1,258 m in the Romanche and Blanco profiles, respectively (Figure 2). The resulting synthetic wavefields can be accurate up to 8.3 Hz, with a minimum sampling of five discretized grid points per wavelength in the simulation (Komatitsch & Tromp, 1999; Komatitsch & Vilotte, 1998). Once the abyssal *T*-waves are computed, we bandpass filter them in the frequency band of 2–4 Hz. Here, we focus on the low-frequency content (i.e., 2–4 Hz), as it has been suggested to be ideal for SOT applications (Callies et al., 2023).

3.2. Sea Surface Roughness

Over the past few decades, profound efforts have been made to understand the sea surface (Ardhuin et al., 2010; Cavaleri et al., 2007), including the modeling of both local wind-driven ocean surface waves and sea swells (Holthuijsen, 2010), with the latter statistically dominating the global sea surface wavefield (Semedo et al., 2011). In principle, the directional wave spectrum of the sea surface can be given as the product of its amplitude spectrum (S(ω)), describing the wave energy as a function of frequency ω, and an angular spreading function (D(θ)), describing the wave directionality with θ as the directional angle. To match in situ and remote sensing measurements, various semi-empirical functions have been suggested for *S(ω)*, including the single-peaked Pierson-Moskowitz type (Pierson Jr. & Moskowitz, 1964) and JONSWAP type (Hasselmann et al., 1980), double-peaked Torsethaugen type (Torsethaugen & Haver, 2004), and others (Elfouhaily et al., 1997; Fung & Lee, 1982; Romeiser et al., 1997). Unlike single-peaked spectra designed for wind sea, the double-peaked Torsethaugen model simultaneously accounts for wind and swell components, representing complex sea states. Meanwhile, a set of analytic forms have been proposed to describe D(θ), including the cosine-squared type (Pierson et al., 1955), Longuet-Higgins type (Longuet-Higgins et al., 1963), and others (Krogstad & Barstow, 1999). Among them, the Longuet-Higgins type is the most widely used due to its simplicity and effectiveness.

Here, we use the Wave Analysis for Fatigue and Oceanography (WAFO) MATLAB toolbox (Brodtkorb et al., 2000) to stochastically model the sea surface roughness. Specifically, we adopt the Torsethaugen model for S(ω) and the Longuet-Higgins type for D(θ). The Torsethaugen model can be empirically parameterized using two variables: SWH and peak period (Torsethaugen & Haver, 2004), both of which can be readily retrieved from ERA5 (Figure 3). Intriguingly, the global field of SWH has strong geographical variations. Equatorial oceans are relatively calm, with a mean SWH of 0–2 m and the highest SWH rarely exceeding 4 m (Figures 3a and 3c). In contrast, oceans at mid- and high-latitudes experience more pronounced sea states due to frequent storms, with a mean SWH of up to 5 m in the Southern Ocean and the highest SWH surging to 20 m in the North Atlantic and Pacific (Figures 3a and 3c). Consequently, SWH in the Romanche TF shows a weak temporal variation ranging between 1 and 3 m (Figure 4a), while SWH in the Blanco TF exhibits substantial seasonal fluctuations, spanning from 1 to 10 m (Figure 4b). Compared to SWH, global peak periods exhibit less spatial variation, with the mean value ranging between 9 and 15 s in most oceans (Figure 3b). Shorter mean periods (<9 s) are observed on the northern side of several Pacific islands (Figure 3b), which can be attributed to their blockage of swell propagation from the Southern Ocean. At the Romanche and Blanco TFs, the temporal variations in peak period fall within a

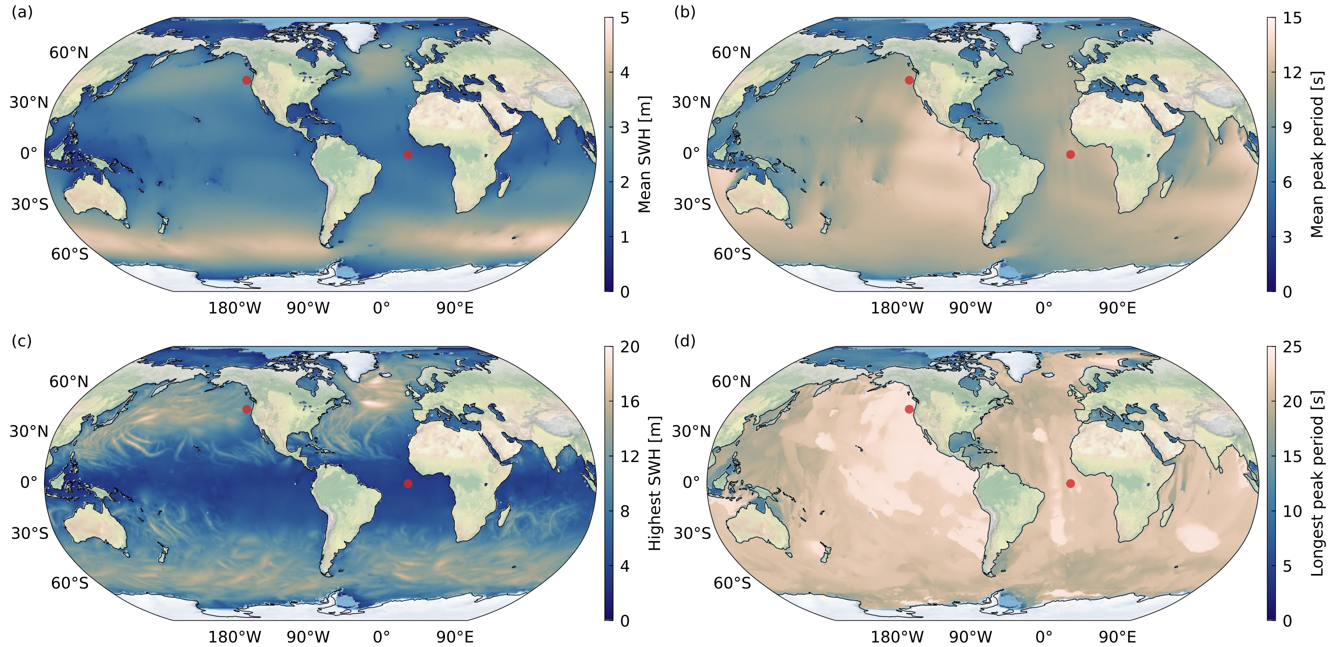

Figure 3. Global sea states. (a). Mean SWH averaged from 2006 to 2023. The two red dots indicate the Romanche and Blanco TFs. (b). Mean peak period averaged from 2006 to 2023. (c). Highest SWH observed between 2006 and 2023. (d). Longest peak period observed between 2006 and 2023.

similar range of 6–22 s (Figures 4c and 4d). Notably, their longest peak periods of 22 s are close to the global maximum of 25 s (Figure 3d).

The realistic SWH and peak period data enable us to simulate various sea states with different directional angles θ. To maximize the effect of the sea surface roughness on abyssal *T*-waves, we solely focus on cases where θ maximizes the sea surface spectral power within the range of 375–750 m, corresponding to the horizontal wavelengths of targeted 2–4 Hz T-waves. The choice of 375–750 m is derived from scattering theory, which suggests that the scattered wave energy directly scales with the spectrum of surface roughness (see Text S1 in Supporting Information S1 for more details; Bataille & Flatté, 1988; Godin, 2021). As an example, given a SWH of 2 m and a peak period of 11 s, a θ of 90° (i.e., ocean surface roughness perpendicular to our profile) yields the highest spectral power within the wavelength range of interest (Figure S1 in Supporting Information S1). Once the random sea surface is generated, we apply a low pass filter of 100 m to avoid aliasing effects in our 50-m SEM meshes. Correspondingly, one random realization of the sea surface roughness for the given SWH and peak period is shown in Figure 4e. Its standard deviation of ∼0.45 m roughly matches a quarter of the 2.0 m SWH (Holthuijsen, 2010). Nonetheless, the spectral power of the sea surface is one to two orders of magnitude lower than that of bathymetry between 375 and 750 m (Figure 4f).

3.3. Internal-Wave-Induced Sound-Speed Perturbations

Small-scale ocean sound-speed fluctuations are primarily due to distortions in the vertical displacements of isotherms by internal waves, which can be reasonably described by the empirical Garrett-Munk (GM) spectrum (Garrett & Munk, 1972; Munk, 1981). While mesoscale eddies generally cause the largest sound-speed perturbations, their length scales are not relevant to our problem here. To model the stochastic internal-wave-induced sound-speed perturbation field, Colosi and Brown (1998) introduced an efficient method based on WKB scaling, which has proven effective in interpreting acoustic measurements (Colosi et al., 1999; Dushaw et al., 2017; Van Uffelen et al., 2009). Specifically, the internal-wave-induced sound-speed perturbation (δc) and density perturbation (δρ) can be linked to the vertical displacement (ζ) of a fluid parcel through Equations 1–4 (Colosi & Brown, 1998).

$$\delta c = c_0\left(\frac{\mu}{g}\right)N^2\zeta \tag{1}$$

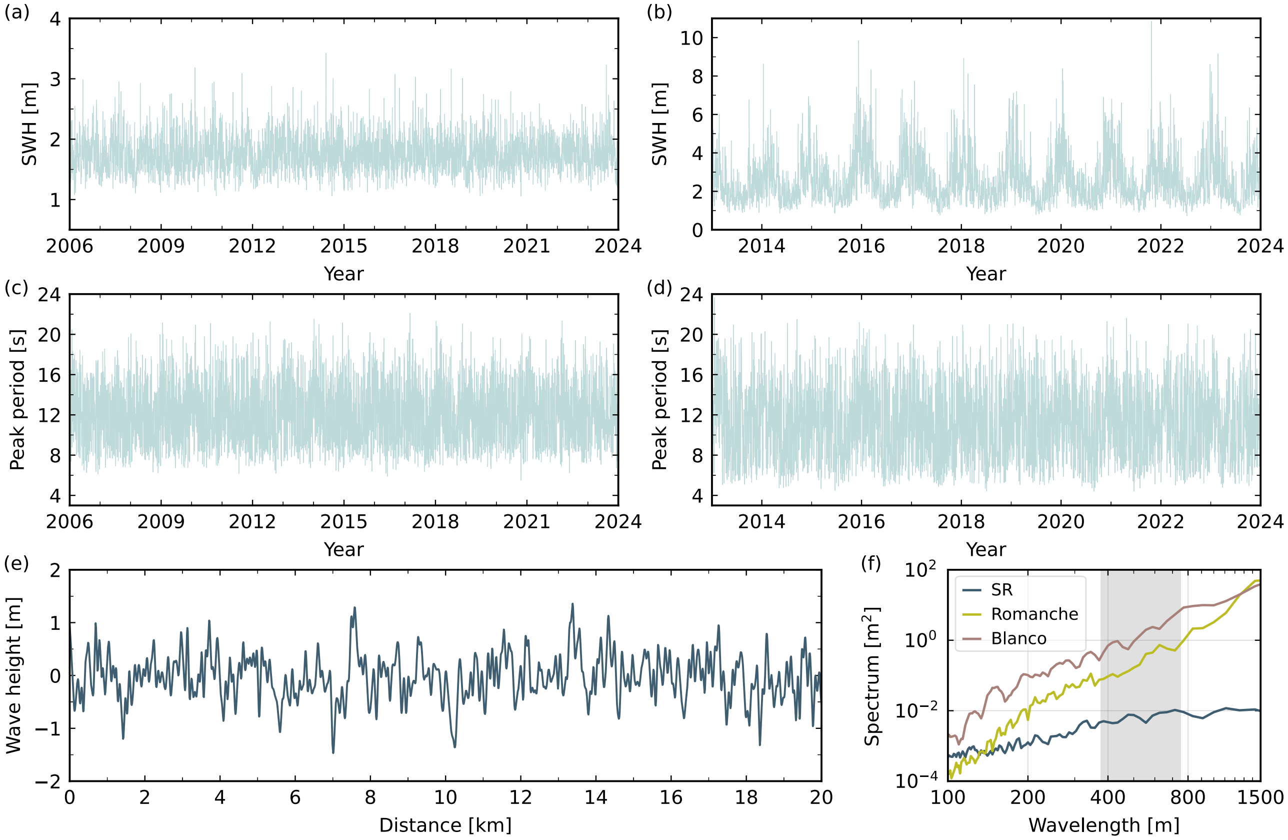

Figure 4. SWH and peak period observations in the Romanche and Blanco TFs and illustration of sea surface roughness. (a). Times series of SWH in the Romanche TF. (b). Time series of SWH in the Blanco TF. (c). Time series of peak period in the Romanche TF. (d). Time series of peak period in the Blanco TF. (e). One realization example of see sea surface roughness with a SWH of 2 m and a peak period of 11 s (f). Spectrum comparison of the sea surface roughness (SR) in (e) and bathymetry profiles in the Romanche and Blanco TFs. The gray band indicates the lateral scale of sea surface roughness (i.e., 375–750 m), to which the 2–4 Hz scattered *T*-waves are most sensitive.

$$\delta\rho = \rho_0 \frac{N^2}{g}\zeta \tag{2}$$

$$\zeta(x, z) = Re\left[\frac{\sqrt{2}N_0}{\pi} b^{3/2}\left(\frac{E}{M}\right)^{1/2} (\Delta k_x)^{1/2} \sum_j \frac{W_j}{\left(j^2 + j_*^2\right)^{1/2}} \sum_{k_x} I(j, k_x)^{1/2} e^{i\phi(j,k_x)} e^{ik_x x}\right] \tag{3}$$

with

$$I(j, k_x) = \sum_{k_y} \frac{k_j\sqrt{k_x^2 + k_y^2}}{\left(k_x^2 + k_y^2 + k_j^2\right)^2}\Delta k_y \tag{4}$$

where c_0 and ρ_0 represent the background sound speed and density, respectively. The gravitational acceleration is $g = 9.81$ m^2/s, and the values $\mu = 24.8$, $j_* = 3$, and $E = 6.3 \times 10^{-5}$ are dimensionless constants. The normalization constant $M \approx \frac{1}{2} j_*^{-2}\left(\pi j_* - 1\right)$. N is the buoyancy frequency, representing the stratification of the water column. Derived from the ECCO salinity and temperature data, N typically peaks in shallow waters and gradually decays with depth (Figure 5a). b = 1,300 m indicates a constant thermocline depth. N_0 is the surface-extrapolated buoyancy frequency, computed as the buoyancy frequency averaged over the thermocline depth, yielding 4.2×10^{-3} rad/s and 4.1×10^{-3} rad/s for the Romanche and Blanco TFs, respectively. k_x and k_y represent the

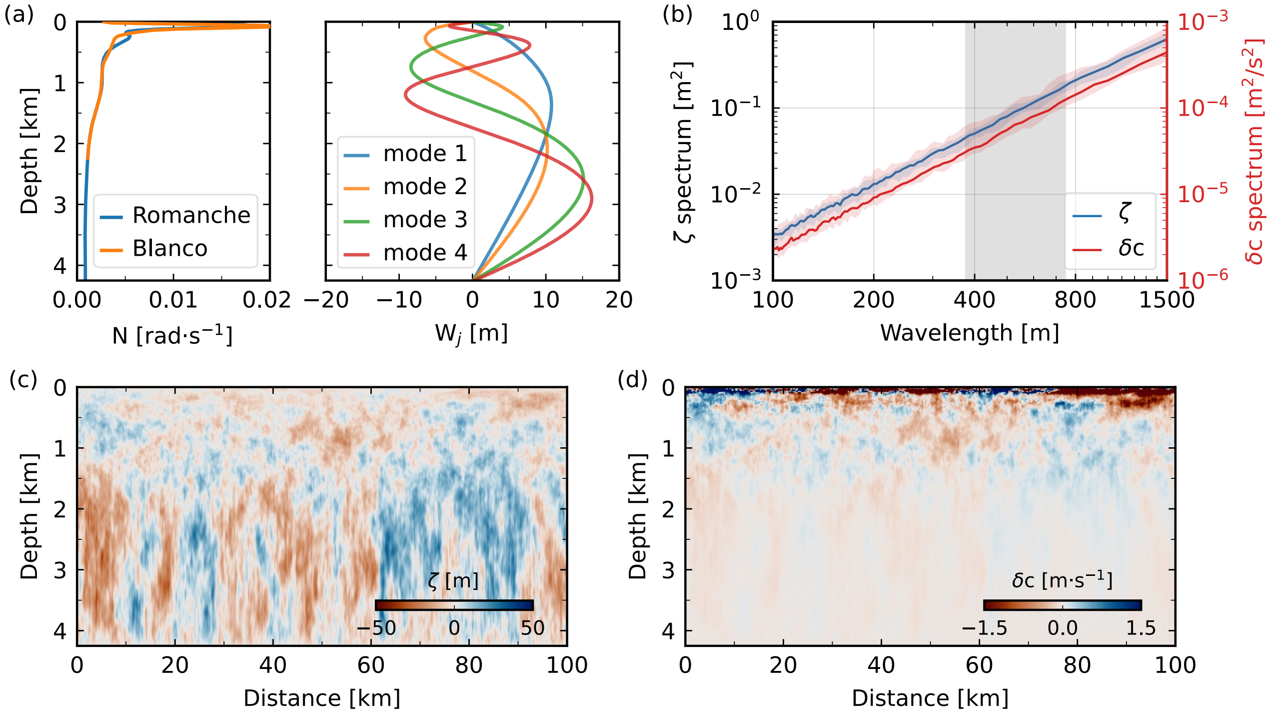

Figure 5. Illustration of internal-wave-induced sound-speed perturbation fields. (a). Realistic buoyancy frequency profiles in the Romanche and Blanco TFs, and eigenvectors of first four vertical modes for the Romanche profile. (b). Spectrum of internal-wave-induced vertical displacement ζ and sound-speed perturbation δc averaged around the SOFAR channel axis (500–1,000 m). The shaded bands associated with the ζ and δc curves indicate their variations at depths of 500–1,000 m. The gray band indicates the lateral scale of sea surface roughness (i.e., 375–750 m), to which the 2–4 Hz scattered *T*-waves are most sensitive. (c). One realization example of ζ for the Romanche profile. (d). Similar to (c) but for δc.

horizontal wavenumbers in the x-direction and y-direction, respectively. k_j is defined as $j\pi f/N_0 b$, where j is the mode number and f is the Coriolis frequency given by $2\Omega sin\vartheta$ with $\Omega = 7.3 \times 10^{-5}\mathrm{s}^{-1}$ denoting the angular velocity of Earth's rotation and ϑ representing the latitude. ϕ describes the random phase with a uniform distribution between 0 and 2π. W_j is the jth internal-wave vertical mode. Unlike the WKB approximation employed by Colosi and Brown (1998) to solve for W_j, here we integrate realistic buoyance frequency profiles into a finite-difference scheme for a more accurate solution of W_j (Figure 5a).

While the GM model provides a good approximation for most of the oceans, it struggles to accurately predict low-frequency internal waves near the Equator (e.g., Romanche TF). This issue arises from the vanishing Coriolis frequency at low latitudes, and it has been suggested to replace f with a constant value at 30°N, denoted as f_{30} (Munk, 1980). Levine (2002) proposed a modified model to closely match the spectral level of the GM model with $f = f_{30}$ and provide a better fit for equatorial observations at frequencies below the semi-diurnal tidal frequency ω_{S2}. Therefore, to describe ζ in the Romanche TF, we employ the GM model with $f = f_{30}$, maintaining consistency with the stochastic internal-wave-induced sound-speed model of Colosi and Brown (1998), but we modify the integral function $I\,(j, k_x)$ formulated in Equation 5 to better account for low-frequency internal waves at Romanche (Levine, 2002).

$$I(j,\,k_x) = \begin{cases} \displaystyle\sum_{k_y} \frac{k_j\sqrt{k_x^2+k_y^2}}{\left(k_x^2+k_y^2+k_j^2\right)^2}\Delta k_y & \mathit{if}\sqrt{k_x^2+k_y^2} > k_{S2} \\ \displaystyle\sum_{k_y} \frac{k_j\sqrt{k_x^2+k_y^2}}{\left(k_x^2+k_y^2+k_j^2\right)^2}\left(1+\frac{k_j}{\sqrt{k_j^2+k_{S2}^2}}\right)\frac{\left(\frac{k_x^2+k_y^2+k_j^2}{k_j^2+k_{S2}^2}\right)^{3/2}}{\left(\frac{k_x^2+k_y^2+k_j^2}{k_j^2+k_{S2}^2}\right)^{5/4}+\left(\frac{k_j^2}{k_j^2+k_{S2}^2}\right)^{1/2}}\Delta k_y & \mathit{if}\sqrt{k_x^2+k_y^2} < k_{S2} \end{cases} \qquad (5)$$

Where k_{S2} represents the semi-diurnal tidal wavenumber, which follows the dispersion relation $k_{S2} = \frac{k_j}{f}\sqrt{\omega_{S2}^2 - f^2}$. Given each k_x and j, $I\,(j, k_x)$ is calculated by summing over the k_y space ranging from -100 to 100 times the maximum of k_x and k_j. Here, the summation range is selected to ensure sufficient contribution from wavelengths in the k_y space. Note that we still use Equation 4 to generate internal-wave-induced sound-speed perturbations for the Blanco TF. With a 20-m grid spacing and a total mode number of 100, our simulated internal waves can displace vertically by up to 50 m in the deep ocean due to its low buoyancy frequency (Figures 5a and 5c). In contrast, the corresponding internal-wave-induced sound-speed perturbation field is most significant in the upper ocean because of the amplification factor of the square of buoyancy frequency (Figures 5a and 5d; Equation 1). In general, the spectral amplitudes of ζ and δc increase with wavelength (Figure 5b).

4. Numerical Simulation Results

Having established the SEM model setup, we now synthesize and compare abyssal T-waves under different hypotheses. The following subsections explore how these scattering mechanisms affect the genesis and propagation of abyssal T-waves, respectively.

4.1. Genesis of Low-Frequency Abyssal T-Waves

To examine the genesis of low-frequency abyssal T-waves, our models can be categorized into four groups: a reference model (Reference) serving as the control group, sea surface roughness (SR) group, internal wave (IW) group, and realistic bathymetry (RB) group (Figure S2 in Supporting Information S1). The Reference model incorporates a flat sea surface, a flat seafloor at the conjugate depth, and a sediment layer with uniform thickness averaged across the profile (Figures S2a–S2b in Supporting Information S1). For the SR, IW and RB groups, we superimpose sea surface roughness, internal-wave-induced sound-speed perturbations, and realistic bathymetry and sediment onto the Reference model within ±50 km from the source, respectively (Figure S2 in Supporting Information S1). The 100-km range is chosen to focus on the source-side excitation of abyssal T-waves and to ensure the generation of coda waves lasting longer than 50 s. To mitigate the potential effects of the abrupt bathymetric cliffs at ±50 km, we apply a cosine taper window to the first and last 10 km of our imposed bathymetry profiles. In the SR group, we use the terms SRmean and SRmax to represent the most common sea state in the source region and the local sea state that maximizes spectral power within our targeted wavelength range, respectively (Figure S3 in Supporting Information S1). For example, SRmean in the Romanche TF corresponds to an SWH and peak period of (2.0 m, 11.0 s), while SRmax corresponds to (4.0 m, 17.0 s) (Table S1 in Supporting Information S1). The Blanco TF exhibits a similar SRmean of (2.0 m, 12.0 s) but a much stronger SRmax of (11.0 m, 16.0 s) (Figure S3; Table S1 in Supporting Information S1). Similarly, IWmean and IWmax are used to denote the standard and maximum GM model, respectively (Table S1 in Supporting Information S1). Given that internal wave observations can deviate from the GM model by a factor of 2–3 (Polzin & Lvov, 2011), we adopt a 10-fold GM spectrum for IWmax to provide an upper bound for the effect of internal wave.

The comparison of synthetic low-frequency abyssal T-waves among different models suggests seafloor scattering as the dominant excitation mechanism (Figure 6). First, the flat-layered Reference model does not produce clear abyssal T-waves near the predicted arrival time (Figure 6). Previous studies have found that the reverberations of seismo-acoustic energy in the water column can generate abyssal T-waves at short distances (<250 km; Chen et al., 2017; Lin et al., 2014). Our simulations of weak T-waves indicate substantial dissipation of acoustic energy through multiple reflections at longer distances (i.e., 935 km for Romanche and 565 km for Blanco), making the Reference models suitable for comparing different scattering mechanisms. Second, SRmean, IWmean and

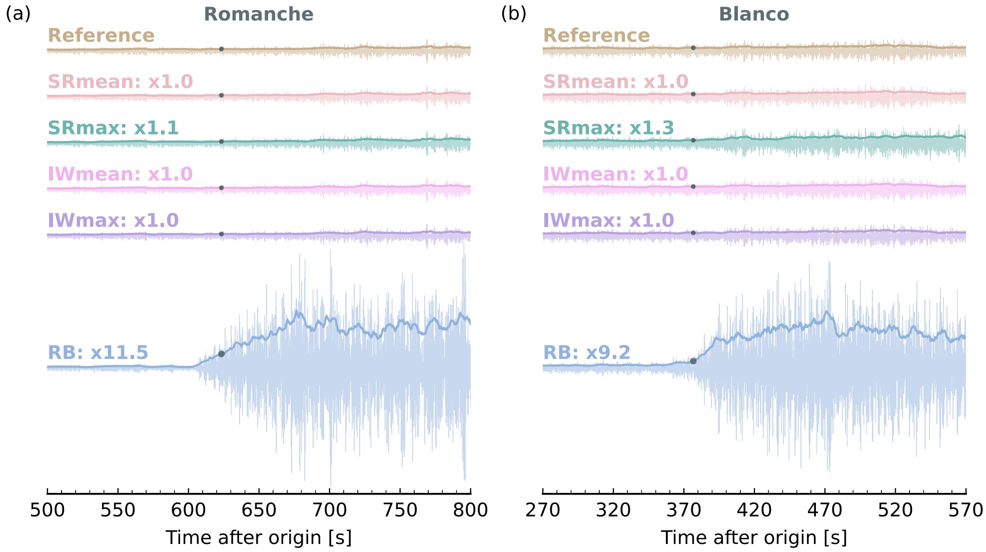

Figure 6. Genesis of low-frequency abyssal *T*-waves in the Romanche and Blanco TFs. (a). Comparisons of 2–4 Hz waveforms for different models in the Romanche TF. The bold solid line represents the envelope of each trace using a 4-s smooth window. Each model is labeled on the left side. The number above each trace indicates the envelope amplitude ratio between each model and the reference trace. The dark dots indicate predicted arrival times of abyssal *T*-waves using a sound speed of 1.5 km/s (b). Similar to (a), but for the Blanco TF.

IWmax models in the Romanche and Blanco TFs also demonstrate minimal low-frequency abyssal *T*-waves (Figure 6), suggesting marginal excitation from the most common sea states and all types of internal waves. Here, all IW models fail to generate abyssal *T*-waves, because long-wavelength-dominated internal waves do not meet the Bragg scattering condition, confirming previous studies (Godin, 2021). Instead, rougher sea states do excite low-frequency abyssal *T*-waves. For example, SRmax models exhibit a 10% amplitude increase within the *T*-wave window for Romanche TF and a 30% increase for Blanco TF at 2–4 Hz (Figure 6). The larger amplitude increase in Blanco TF can be attributed to its more intense local sea state in SRmax (Table S1 in Supporting Information S1). Lastly, RB models produce the strongest low-frequency abyssal *T*-waves among all models, with amplitudes boosted by a factor of 11.0 and 9.2 for Romanche and Blanco TFs, respectively (Figure 6). The amplitude increases in RB models significantly surpass those observed in SRmax. These waves have clear onsets near the predicted arrival time (Figure 6), confirming seafloor scattering at the source side. While the RB model for Romanche TF exhibits a time difference of ~20 s between the predicted and simulated onset (Figure 6), the corresponding spatial distance is ~30 km, still within our embedded bathymetry range of 50 km. Furthermore, to explore the effect of source depth on the generation of low-frequency abyssal *T*-waves, we conduct additional simulations with source depths of 20 km for the Romanche profile and 15 km for the Blanco profile. The depths of 20 and 15 km approximately correspond to the 600°C isotherms (or seismicity cutoff depth) at these sites (Braunmiller & Nábělek, 2008; Kuna et al., 2019; Schlaphorst et al., 2023; Yu et al., 2021; Zang et al., 2024). Similarly, the seafloor scattering generates synthetic *T*-waves much stronger than that by sea surface roughness and internal waves (Figure S4 in Supporting Information S1). Therefore, the seafloor proves to be 1–2 orders of magnitude more effective than the sea surface and internal waves in generating low-frequency abyssal *T*-waves.

In addition, it should be noted that the current global seafloor map lacks adequate resolution at short scales (<1 km), as high-resolution bathymetry data are only available in specific survey regions. For instance, ship-based multibeam data in Chain TF capture significant small-scale features compared to nearby Romanche TF, where limited high-resolution sonar data is integrated in GMRT (Harmon et al., 2018; Ryan et al., 2009; Figure S5 in Supporting Information S1). To investigate the effects of short-scale bathymetry on the genesis of low-frequency abyssal *T*-waves, we replace bathymetry with wavelengths shorter than 2 km in the Romanche and Blanco TFs with that of Chain TF within ±50 km from the source (Figure S5a in Supporting Information S1). The choice of 2 km is to better understand the role of non-geometric scattering due to seafloor features comparable to the wavelength of low-frequency abyssal *T*-waves. In numerical simulations, the meshes are generated to exactly honor the bathymetry and excludes the sediment layer to solely focus on seafloor scattering. Notably, the

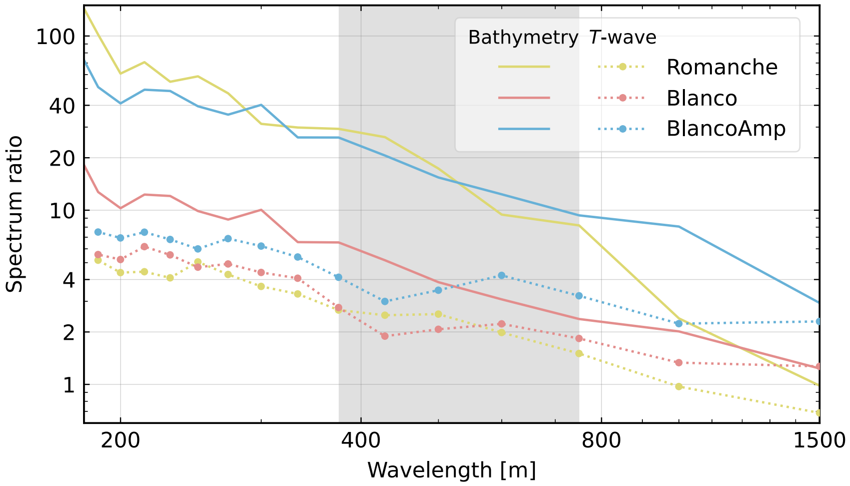

Figure 7. Effects of short-scale bathymetry on the genesis of abyssal *T*-waves. The solid lines indicate the spectrum ratio between modified and original bathymetry for Romanche, Blanco and BlancoAmp cases. The dotted lines represent corresponding abyssal *T*-wave spectrum ratios. The gray shaded region indicates the lateral scale of sea surface roughness (i.e., 375–750 m), to which the 2–4 Hz scattered *T*-waves are most sensitive.

modified bathymetric profiles enrich small-scale features, with spectral amplitudes increasing from 2-fold at 800 m to 10-fold at 200 m for Blanco, and from 2-fold at 800 m to 60-fold at 200 m for Romanche (Figure 7). This modified bathymetry, incorporating more details at short scale, proves to be more efficient in exciting abyssal *T*-waves across a broad frequency range (i.e., 1–8 Hz corresponding to 200–1,500 m). For both Romanche and Blanco cases, the spectral amplitudes of abyssal *T*-waves double at 2–4 Hz and exhibit a more pronounced increase by a factor of 4–6 at higher frequencies (>4 Hz; Figure 7). To further test the sensitivity to short-scale seafloor roughness, we conduct an additional simulation by doubling the short-scale bathymetry of the modified Blanco profile, referred to as BlancoAmp. Compared to the modified Blanco case, BlancoAmp excites stronger abyssal *T*-waves in the frequency band of 1–8 Hz, with spectral amplitudes doubling further at 2–4 Hz (Figure 7). Although the true small-scale seafloor roughness at Romanche and Blanco TFs remains unknown, it is believed to be stronger than that represented in the current global bathymetry map, which lacks small-scale features. Hence, the amplitudes of seafloor scattering *T*-waves estimated in Figure 6 should be considered as a conservative estimate, and the true seafloor scattering would likely be even stronger.

4.2. Propagation of Low-Frequency Abyssal *T*-Waves

Although sea surface and internal waves play minor roles in the genesis of low-frequency abyssal *T*-waves, their effects on propagation remain unquantified. We first simulate low-frequency abyssal *T*-waves for a Reference model that incorporates realistic bathymetry and sediment along the entire profile (Figures S6a–S6b in Supporting Information S1). Notably, this new Reference model differs from the previous one (Figures S2a-S2b in Supporting Information S1), since the dominance of seafloor scattering in exciting low-frequency abyssal *T*-waves has been demonstrated. When applying realistic bathymetry to the entire profile, the resulting low-frequency abyssal *T*-waves exhibit a more spindle-like-shape with unclear onsets compared to those in previous RB models (Figures 8a and 8d vs. 6), indicating that seafloor scattering is not only limited to the source side. Meanwhile, SRmean, SRmax, IWmean and IWmax models are implemented throughout the entire profiles in Romanche and Blanco TFs (Figure S6; Table S1 in Supporting Information S1). To statistically quantify the effects of sea surface and internal waves, we generate 50 realizations for each model type. In each realization, we cross-correlate the corresponding *T*-wave with the reference *T*-wave to measure waveform coherence and time shift using a consecutive moving window. At a given time, a 30-s window with 15 s before and after it is used for the cross-correlation calculation.

Our simulation results indicate that sea surface roughness and internal waves do not substantially distort low-frequency abyssal *T*-waves during propagation (Figure 8). Specifically, the synthetic *T*-waves of SRmean and SRmax models in the Romanche TF are identical to the reference waveform at 2–4 Hz (Figures 8a and 8b). In the Blanco TF, where the sea state is rougher (Table S1 in Supporting Information S1), SRmax models exhibit

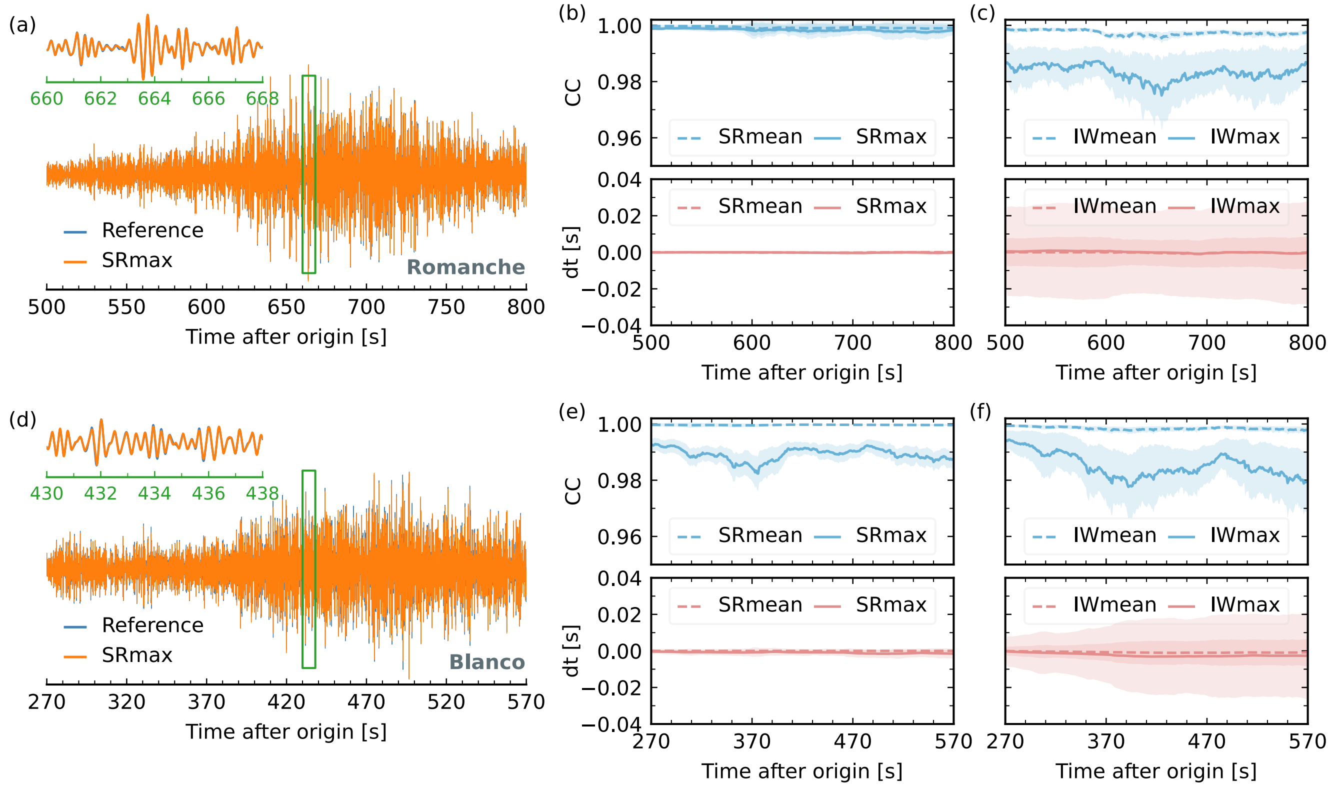

Figure 8. Effects of sea surface roughness and internal waves on the propagation of low-frequency abyssal *T*-waves. (a). Comparisons of 2–4 Hz waveforms between Reference and SRmax models in the Romanche TF. (b). Cross-correlation coefficient (CC) and time shift measurements as a function of time for SRmean and SRmax models in the Romanche TF. The shaded area indicates variability of 50 realizations. (c). Similar to (b), but for IWmean and IWmax models in the Romanche TF. (d). Comparisons of 2–4 Hz waveforms between Reference and SRmax models in the Blanco TF. (e). Similar to (b), but for SRmean and SRmax models in the Blanco TF. (d). Similar to (e), but for IWmean and IWmax models in the Blanco TF.

slightly lower cross-correlation coefficients (CC) but negligible travel time changes (Figures 8d and 8e). In comparison, internal waves not only reduce waveform coherence but also introduce travel time changes with greater variability (Figures 8c and 8f). Over a distance range of 560–960 km, increasing the spectral energy of internal waves can lead to abyssal *T*-wave travel time perturbations of up to 0.02 s (Figure 8f). However, the 0.02 s variation is still smaller than the previously observed internal-tide-induced time shifts of 0.1–0.2 s over a distance range of 1,500–2,000 km in the Northwest Pacific (Sugioka et al., 2005). Such discrepancy could arise from 2 to 3 orders of magnitude stronger M_2 internal tides generated by predominant bathymetric features along the Izu-Bonin-Mariana Ridge (Niwa & Hibiya, 2001), which are not accounted for in our standard and enhanced GM models. Except in regions with abnormally strong M_2 internal tides, *T*-wave travel time perturbations due to internal waves and sea surface roughness are relatively small compared to those caused by ocean temperature changes. For example, assuming a sound speed increase of 4.5 m/s per 1 K rise in ocean temperature, a 0.02 s time shift corresponds to an ocean temperature variation of 10 and 17 mK in Romanche and Blanco TFs, respectively. For comparison, basin-scale ocean temperature can fluctuate on the order of 100 mK over a seasonal scale (Peng et al., 2024; Wu et al., 2020). In addition, these dynamics behave as random processes and, if desired, can be treated as the measurement errors in SOT applications (Callies et al., 2023; Peng et al., 2024; Wu et al., 2023).

4.3. Effects of Extreme Sea State

While local sea states in the Romanche and Blanco TFs demonstrate negligible effects on the genesis and propagation of low-frequency abyssal *T*-waves compared to seafloor scattering, rougher sea surface in other regions would produce stronger scattering waves. To assess those scattering, we build SRGmax models, which reflect the maximum spectral power of global sea state at the *T*-wave sensitive wavelengths. Specifically, SRGmax is parameterized with a peak period of 18 s and an SWH of 20 m (Figure S7; Table S1 in Supporting Information S1). The 20 m SWH in SRGmax is almost double that of SRmax in Blanco TF and five times that of

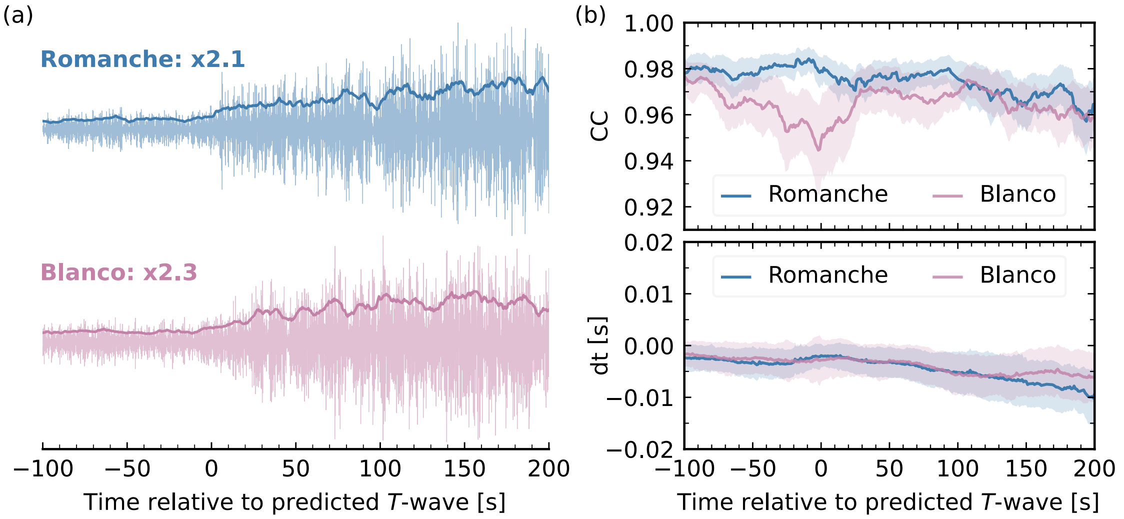

Figure 9. Effects of SRGmax on the genesis and propagation of low-frequency abyssal *T*-waves. (a). Synthetic 2–4 Hz abyssal *T*-waves for SRGmax models in the Romanche and Blanco TFs, with SRGmax applied within ±50 km from the source. The number above the trace indicates the envelope amplitude ratio between SRGmax and Reference models in Figure 6b. Cross-correlation coefficient (CC) and time shift measurements as a function of time for SRGmax models in the Romanche and Blanco TFs. Here, SRGmax is applied along the entire propagation path. The shaded area represents measurement variability of 50 realizations.

SRmax in Romanche TF (Table S1 in Supporting Information S1). Implementing SRGmax within ±50 km from the source excites stronger low-frequency abyssal *T*-waves, amplifying the reference amplitude by a factor of 2.1 for Romanche TF and 2.3 for Blanco TF (Figure 9a). Nonetheless, abyssal *T*-waves in SRGmax models remain substantially weaker than those in RB models, implying a secondary role of sea surface scattering (Figure 6 vs. Figure 9a). Similarly, applying SRGmax along the propagation path does not significantly distort reference waveforms, with *T*-wave CCs above 0.92 and time shifts within 0.015 s (Figure 9b). Thus, we conclude that the effects of sea surface roughness scattering on *T*-wave are weak even for the strongest sea surface roughness of the global ocean. It is noteworthy that SRGmax models tend to exhibit systematical negative time shifts (*T*-waves arriving early due to sea surface scattering) for both Romanche and Blanco TFs (Figure 9b), contrary to the expected randomness. This tendence is a simulation artifact, because we treat the sound speed as a static field and speeds of the SEM meshes are simply interpolated from a fixed-grid 2D model. With the sound speed increasing toward the sea surface (Figure 2), the interpolation scheme used in our model setup yields slightly faster sound speeds near the surface when sea surface roughness is introduced.

5. Repeatability of Low-Frequency Abyssal *T*-Waves

Our numerical findings in the previous section support seafloor scattering as the predominant mechanism governing the genesis of low-frequency abyssal *T*-waves. Despite the use of reasonable parameters, it is worth noting that the quantitative comparison of numerical results may be affected by uncertainties in the model space, such as crustal and sediment properties (Jamet et al., 2013). While conducting thorough parameter testing could theoretically address this issue, such an approach is prohibitive due to its computational expense. Instead, we leverage observational data from repeating earthquakes to independently confirm seafloor scattering as the primary mechanism. This approach hinges on the concept of examining the repeatability of abyssal *T*-waves: seafloor scattering consistently generates repeatable *T*-wave signatures, whereas variations in sea surface roughness and internal waves over time would not yield high coherency.

In the Romanche and Chain TFs, the ISC catalog reports ∼1000 events between 2006 and 2023, when both DBIC and H10N2 data are available. However, our initial attempt using the ISC catalog only identifies seven useable repeating pairs, which yields limited statistical significance to explore the repeatability of abyssal *T*-waves. To detect missing repeating earthquakes, we apply a template matching approach using ISC-cataloged events as templates (Li et al., 2021; Wu et al., 2023). Specifically, we retrieve continuous vertical-component waveforms from DBIC in 2006–2023, remove their instrument response and linear trend, and filter them to 2–4 Hz. A new event is identified once its waveform CC surpasses a threshold of 0.6. Given the new detections, *P*-wave CCs are

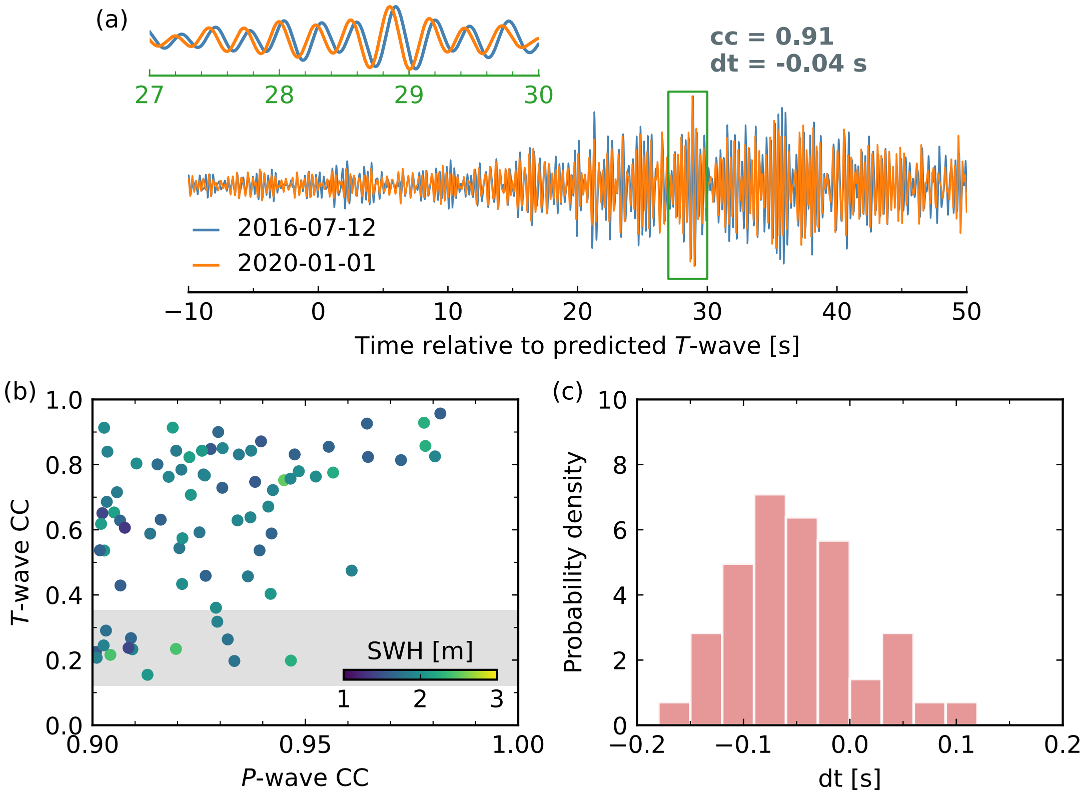

Figure 10. Repeatability of low-frequency abyssal *T*-waves in the Romanche TF. (a). Example of repeating abyssal *T*-waves with CC and time shift measurements noted in the top-right corner. The top-left inset panel provides a zoom-in view of a 3-s window. (b). Abyssal *T*-wave CC as a function of *P*-wave CC for repeating pairs. The gray band indicates the *T*-wave CC range if sea surface scattering dominates the genesis and propagation of abyssal *T*-waves. (c). Histogram of time shift measurements. Only repeating *T*-waves with CC above 0.6 are used.

calculated for all event pairs using a 50-s window cut from −3 to 47 s relative to the predicted arrival. After removing obvious false detections (e.g., sudden spikes due to instrument issues), we document a total of 76 repeating events with *P*-wave CCs higher than 0.9 at DBIC (Figure 1b). Intriguingly, no repeating events are found on the west side of the Romanche TF, likely due to their longer distances to DBIC and therefore lower SNRs at DBIC (Figure 1b). Having suitable *P*-wave stations is crucial for detecting repeating earthquakes in remote areas. Nonetheless, all identified repeating events on the east side of the Romanche TF generate low-frequency abyssal *T*-waves with high signal-to-noise ratios at H10N2 (Figure 10a), enabling us to evaluate the repeatability. For each pair, we cut the repeating abyssal *T*-waves into a 60-s window to determine waveform coherence and time shift (Figure 10a).

As an example, the repeating *T*-waves in the Romanche TF—one on 12 July 2016 and the other on 1 January 2020—demonstrate evident repeatability with a CC of 0.91 and a time shift of −0.04 s in the frequency band of 2–4 Hz (Figure 10a). Given the random sea state, such high waveform similarity rules out the hypothesis of sea surface scattering dominating the genesis and propagation of low-frequency abyssal *T*-waves. To further quantify the repeatability of the sea surface roughness scattering waves, we conduct 20 simulations of random sea surface roughness by enhancing SRmean 20-fold. While the 20-fold increase in SRmean is unrealistic (Figure 3), we use it here solely to amplify the sea surface scattering signals and ensure an accurate assessment. The 20 simulations result in a total of 190 repeating pairs, with repeating *T*-wave CCs ranging from 0.12 to 0.35 (Figure 10b). However, 82% of identified repeating *T*-wave observations exhibit high repeatability with CCs above 0.35 (Figure 10b). There remain 14 repeating pairs that exhibit low *T*-wave CCs falling within the sea-surface-affected range (Figure 10b). But we do not observe a significant correlation between sea state and repeating *T*-wave CCs, since the Equatorial oceans do not exhibit strong seasonality in SWH (Figures 4a and 10b). Therefore, we attribute the low *T*-wave CCs to the events not precisely repeating, due to the use of a single *P*-wave station for detection

(Gao et al., 2021). To support this interpretation, we observed two lines of evidence. First, we note that the repeating pairs with low *T*-wave CCs exhibit relatively low *P*-wave CCs (<0.95) at DBIC, while events with *P*-wave CCs above 0.96 all exhibit high *T*-wave CCs (>0.75; Figure 10b). Second, some of these events generate high-quality but less coherent *P*-waves with CC below 0.9 at hydrophone H10N2, supporting our argument regarding the low repeatability of *T*-wave CCs (Figure S8 in Supporting Information S1). Meanwhile, a previous study has suggested that 3D multipathing effects due to oceanographic variations could also reduce the coherence of repeating *T*-waves in the Kuroshio Extension region (Peng et al., 2024). However, such 3D effects are regionally dependent and are unlikely to be applicable to the Equatorial Atlantic, as the lateral heterogeneity observed in the Kuroshio Extension region is stronger by at least an order of magnitude (Peng et al., 2024). The resulting time shifts vary from −0.17 to 0.11 s, much larger than the internal-wave-induced variability (Figure 8c vs. Figure 10c). Such time shift variation roughly corresponds to an average ocean temperature change of 91 mK to −59 mK, a reasonable range for long-range SOT (Wu et al., 2023). Furthermore, we observe that most time shifts tend to be negative (i.e., the latter repeating *T*-wave travels faster than the early one; Figure 10c), which may reflect a warming trend in Equatorial Atlantic between 2006 and 2023 (Desbruyères et al., 2017; Purkey & Johnson, 2010; von Schuckmann et al., 2009). In addition to H10N2, there are five other CTBTO hydrophones near Ascension Island (Figure S9 in Supporting Information S1). Together, these six hydrophones form two triangular networks, spaced approximately 130 km apart (Figure S9 in Supporting Information S1). Compared to H10N2, the repeating abyssal *T*-waves at four other hydrophones (i.e., H10N1, H10N3, H10S2, and H10S3) show similar repeatability and consistent time shift measurements (Figure S10 in Supporting Information S1). The hydrophone H10S1 exhibits relatively low repeatability, which can be attributed to the low signal-to-noise ratios of abyssal *T*-waves (Figure S11 in Supporting Information S1). Hence, our observation of highly repeatable abyssal *T*-waves indicates the feasibility of SOT applications leveraging repeating earthquakes in deep oceans (e.g., mid-ocean ridges, transform faults and outer rise of subduction zone).

In contrast to the limited number of ISC-documented repeating earthquakes in the Romanche TF, we identify 45 repeating pairs in Blanco TF directly from the ISC catalog between 2013 and 2023 without template matching. Here, a more stringent criterion is applied to enhance the repeating event detection, requiring *P*-wave CCs to exceed a threshold of 0.9 at two *P*-wave stations (Figure 1c). Similar to the Romanche TF, repeating events are mostly detected on the east side of the Blanco TF, likely due to their short distances to *P*-wave stations (Figure 1c). Out of the 45 repeating pairs in the Blanco TF, 44 pairs demonstrate remarkable repeatability with *T*-wave CCs above that of sea surface scattered waves (Figures 11a and 11b), favoring the seafloor scattering hypothesis. Also, the *T*-wave CCs in Blanco are generally higher than those in Romanche, and fewer repeating pairs fall within the sea-surface-affected range (Figure 10 vs. Figure 11b). Strikingly, the repeating pair with lowest *T*-wave CCs occurred during calm ocean conditions, while those that occurred during rougher sea states demonstrate much higher repeatability of abyssal *T*-waves (Figure 11b), further ruling out sea surface scattering as a significant role. If we use a *T*-wave CC threshold of 0.6 (Wu et al., 2020), over 75% of the repeating pairs meet the criterion, making them suitable for SOT analysis (Figure 11c). The corresponding time shift varies between −0.11 and 0.08 s (Figure 11c), equivalent to an ocean temperature change from 97 mK to −70 mK.

6. Discussion and Conclusions

The dominant role of seafloor scattering in generating low-frequency abyssal *T*-waves ensures high repeatability of these waves from mid-ocean ridges and transform faults, greatly broadening the useable data spectrum for SOT applications. However, many repeating earthquakes that occurred in the remote ocean remain missing in the current earthquake catalogs. Efforts to detect these events and obtain high-quality *P*-wave data are crucial to ensure the feasibility of SOT. Understanding the roles of seafloor roughness, sea surface roughness, and internal waves also proves crucial when applying low-frequency abyssal *T*-waves to estimate source parameters (Okal, 2008; Slack et al., 1999; Yun et al., 2022). Currently, oceanic earthquake locations are typically determined by analyzing the arrival times of *T*-wave envelop peaks (Okal, 2008; Slack et al., 1999). But the complicated 3-D effects of seafloor roughness on *T*-waves could lead to variation in the envelop shape, consequently introducing considerable uncertainties in event location estimate (de Groot-Hedlin & Orcutt, 2001; Lecoulant et al., 2019; Oliveira & Lin, 2019; Yang & Forsyth, 2003). While these complexities can be addressed through numerical simulations (Lecoulant et al., 2021), such endeavors pose challenges in computational cost and the need for high-resolution bathymetry and crust structure models. An alternative and more feasible approach could involve utilizing empirical excitation functions from nearby events to improve the relative location and

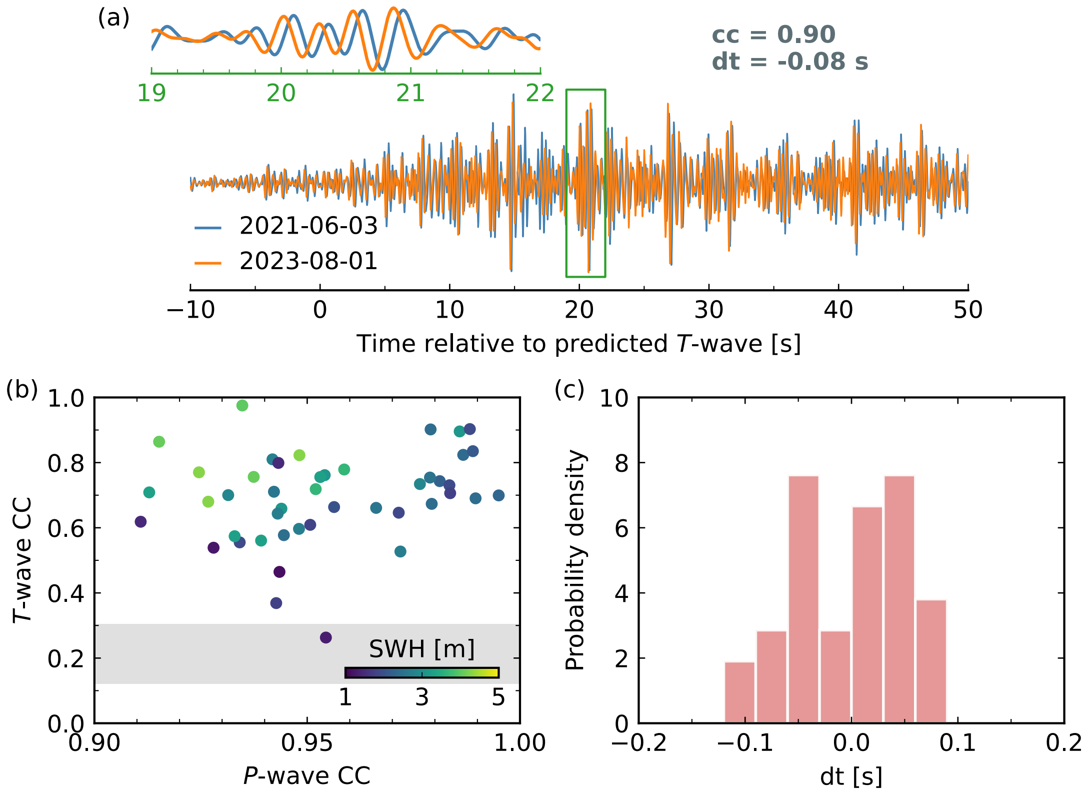

Figure 11. Repeatability of low-frequency abyssal *T*-waves in the Blanco TF. (a). Example of repeating abyssal *T*-waves with CC and time shift measurements noted in the top-right corner. The top-left inset panel provides a zoom-in view of a 3-s window. (b). Abyssal *T*-wave CC as a function of *P*-wave CC for repeating pairs. The gray band indicates the *T*-wave CC range if sea surface scattering dominates the genesis and propagation of abyssal *T*-waves. (c). Histogram of time shift measurements. Only repeating *T*-waves with CC above 0.6 are used.

magnitude estimates (Yang & Forsyth, 2003). However, if sea surface or interval waves were to substantially affect abyssal *T*-waves, neither numerical modeling nor the empirical calibration approach is viable, especially given their dynamic nature over time. Fortunately, this concern has been mitigated, as we have demonstrated the marginal impact from both sea surface roughness and internal waves.

In this study, we use numerical simulations and repeating earthquakes to interrogate the genesis and propagation hypotheses of low-frequency abyssal *T*-waves, including seafloor scattering, sea surface scattering, and internal wave scattering. By incorporating realistic bathymetry, sea states, and internal-wave-induced sound-speed perturbations into the Romanche and Blanco profiles, our simulations underscore the dominant role of seafloor scattering in the genesis and propagation of low-frequency abyssal *T*-waves, with the sea surface and internal waves contributing marginally. Increasing sea surface roughness and internal wave energy can slightly distort low-frequency abyssal *T*-waves, leading to time shift variations of up to 0.02 s. These time shift variations can be considered as measurement uncertainties in SOT applications. In addition to numerical simulations, the high repeatability of low-frequency abyssal *T*-waves observed in the Romanche, Chain, and Blanco TFs further points to seafloor scattering as the primary mechanism, as random sea states and internal waves would result in low waveform coherence of repeating abyssal *T*-waves. The dominance of seafloor scattering enables the use of repeating earthquakes in mid-ocean ridges, transform faults and outer rises for SOT, greatly expanding the useable data spectrum to constrain ocean temperature changes. Our repeating abyssal *T*-wave observations in the Romanche TF exhibit negative travel changes for most repeating pairs. While this increase in sound speed may be attributed to long-term ocean warming, it is important to account for other factors such as measurement uncertainties, seasonal variations, and other short-term changes before drawing definitive conclusions. Given the substantial contributions of short-scale bathymetry features in generating abyssal *T*-waves, further investigations incorporating high-resolution seafloor features are warranted to evaluate the corresponding effects and uncertainties in earthquake source parameter estimation.

Data Availability Statement

The GMRT bathymetry data can be downloaded from https://www.gmrt.org/, and the multibeam bathymetry data for Chain TF is available at https://doi.org/10.5281/zenodo.13543715 (Shen, 2024). The earthquake catalog is downloaded from the International Seismological Centre (http://www.isc.ac.uk/). The significant wave height and peak period data can be accessed from the ERA5 hourly data on single levels at https://cds.climate.copernicus.eu/portfolio/dataset/reanalysis-era5-single-levels. The ECCO temperature and salinity data are available at https://podaac.jpl.nasa.gov/dataset/ECCO_L4_TEMP_SALINITY_05DEG_DAILY_V4R4. The hydrophone data at H10N2 before 2015 are available from the CTBTO upon request and signing a confidentiality agreement to access the virtual Data Exploitation Centre (vDEC; https://www.ctbto.org/resources/for-researchers-experts/vdec). All other seismic and hydrophone data are downloaded from the IRIS Data Management Center (https://ds.iris.edu/ds/nodes/dmc/), including seismic networks GT (Albuquerque Seismological Laboratory (ASL)/USGS, 1993), IM (Various Institutions, 1965; for H10N2 after 2015), NV (Ocean Networks Canada, 2009), and PB (https://www.fdsn.org/networks/detail/PB/). The WAFO MATLAB toolbox is downloaded at https://github.com/wafo-project/wafo. The code for processing seismic data is available at https://github.com/joernc/SOT.

Acknowledgments

This project is supported by the National Science Foundation Grant OCE-2241663. We thank the Woods Hole Oceanographic Institution for making high-performance computing resources available for conducting this research. This work also used the Delta system at the National Center for Supercomputing Applications through allocation EES230037 from the Advanced Cyberinfrastructure Coordination Ecosystem: Services and Support (ACCESS) program, which is supported by National Science Foundation grants #2138259, #2138286, #2138307, #2137603, and #2138296.

References

Abercrombie, R. E., & Ekström, G. (2001). Earthquake slip on oceanic transform faults. *Nature*, *410*(6824), 74–77. https://doi.org/10.1038/35065064

Albuquerque Seismological Laboratory (ASL)/USGS. (1993). Global telemetered seismograph network (USAF/USGS) [Dataset]. *International Federation of Digital Seismograph Networks*. https://doi.org/10.7914/SN/GT

Ardhuin, F., Rogers, E., Babanin, A. V., Filipot, J.-F., Magne, R., Roland, A., et al. (2010). Semiempirical dissipation source functions for ocean waves. Part I: Definition, calibration, and validation. *Journal of Physical Oceanography*, *40*(9), 1917–1941. https://doi.org/10.1175/2010JPO4324.1

Barnes, C. R., Best, M. M., & Zielinski, A. (2008). The NEPTUNE Canada regional cabled ocean observatory. *Technology*, *50*(3), 10–14.

Bataille, K., & Flatté, S. M. (1988). Inhomogeneities near the core-mantle boundary inferred from short-period scattered PKP waves recorded at the Global Digital Seismograph Network. *Journal of Geophysical Research*, *93*(B12), 15057–15064. https://doi.org/10.1029/JB093iB12p15057

Biot, M. A. (1952). The interaction of Rayleigh and Stoneley waves in the ocean bottom. *Bulletin of the Seismological Society of America*, *42*(1), 81–93. https://doi.org/10.1785/BSSA0420010081

Bird, P. (2003). An updated digital model of plate boundaries. *Geochemistry, Geophysics, Geosystems*, *4*(3). https://doi.org/10.1029/2001GC000252

Boettcher, M. S., Hirth, G., & Evans, B. (2007). Olivine friction at the base of oceanic seismogenic zones. *Journal of Geophysical Research*, *112*(B1). https://doi.org/10.1029/2006JB004301

Bonatti, E., Ligi, M., Gasperini, L., Peyve, A., Raznitsin, Y., & Chen, Y. J. (1994). Transform migration and vertical tectonics at the Romanche fracture zone, equatorial Atlantic. *Journal of Geophysical Research*, *99*(B11), 21779–21802. https://doi.org/10.1029/94JB01178

Bondár, I., & Storchak, D. (2011). Improved location procedures at the international seismological Centre. *Geophysical Journal International*, *186*(3), 1220–1244. https://doi.org/10.1111/j.1365-246X.2011.05107.x

Bottero, A. (2018). *Full-wave numerical simulation of T-waves and of moving acoustic sources*. (Doctoral dissertation). Université Aix Marseille.

Bottero, A., Cristini, P., & Komatitsch, D. (2020). On the influence of slopes, source, seabed and water column properties on T waves: Generation at shore. *Pure and Applied Geophysics*, *177*(12), 5695–5711. https://doi.org/10.1007/s00024-020-02611-z

Braunmiller, J., & Nábělek, J. (2008). Segmentation of the Blanco Transform Fault Zone from earthquake analysis: Complex tectonics of an oceanic transform fault. *Journal of Geophysical Research*, *113*(B7). https://doi.org/10.1029/2007JB005213

Brodtkorb, P. A., Johannesson, P., Lindgren, G., Rychlik, I., Rydén, J., & Sjö, E. (2000). WAFO-a Matlab toolbox for analysis of random waves and loads. In *The tenth international Ocean and polar engineering conference* (Vol. 3, pp. 343–350). Seattle.

Callies, J., Wu, W., Peng, S., & Zhan, Z. (2023). Vertical-slice ocean tomography with seismic waves. *Geophysical Research Letters*, *50*(8), e2023GL102881. https://doi.org/10.1029/2023GL102881

Cavaleri, L., Alves, J.-H. G. M., Ardhuin, F., Babanin, A., Banner, M., Belibassakis, K., et al. (2007). Wave modelling – The state of the art. *Progress in Oceanography*, *75*(4), 603–674. https://doi.org/10.1016/j.pocean.2007.05.005

Chen, C.-W., Huang, C.-F., Lin, C.-W., & Kuo, B.-Y. (2017). Hydroacoustic ray theory-based modeling of T wave propagation in the deep ocean basin offshore eastern Taiwan. *Geophysical Research Letters*, *44*(10), 4799–4805. https://doi.org/10.1002/2017GL073516

Chiu, C. (1994). Downslope modal energy conversion. *Journal of the Acoustical Society of America*, *95*(3), 1654–1657. https://doi.org/10.1121/1.408552

Colosi, J. A. (2016). *Sound propagation through the stochastic ocean*. Cambridge University Press.

Colosi, J. A., & Brown, M. G. (1998). Efficient numerical simulation of stochastic internal-wave-induced sound-speed perturbation fields. *Journal of the Acoustical Society of America*, *103*(4), 2232–2235. https://doi.org/10.1121/1.421381

Colosi, J. A., Flatté, S. M., & Bracher, C. (1994). Internal-wave effects on 1000-km oceanic acoustic pulse propagation: Simulation and comparison with experiment. *Journal of the Acoustical Society of America*, *96*(1), 452–468. https://doi.org/10.1121/1.411331

Colosi, J. A., Scheer, E. K., Flatté, S. M., Cornuelle, B. D., Dzieciuch, M. A., Munk, W. H., et al. (1999). Comparisons of measured and predicted acoustic fluctuations for a 3250-km propagation experiment in the eastern North Pacific Ocean. *Journal of the Acoustical Society of America*, *105*(6), 3202–3218. https://doi.org/10.1121/1.424650

Coyne, J., Bobrov, D., Bormann, P., Duran, E., Grenard, P., Haralabus, G., et al. (2012). Ctbto: Goals, networks, data analysis and data availability. *Deutsches GeoForschungsZentrum GFZ*, *2*(NMSOP-2), 1–41.

de Groot-Hedlin, C. D., & Orcutt, J. A. (1999). Synthesis of earthquake-generated T-waves. *Geophysical Research Letters*, *26*(9), 1227–1230. https://doi.org/10.1029/1999GL900205

de Groot-Hedlin, C. D., & Orcutt, J. A. (2001). Excitation of T-phases by seafloor scattering. *Journal of the Acoustical Society of America*, *109*(5), 1944–1954. https://doi.org/10.1121/1.1361057

Desbruyères, D., McDonagh, E. L., King, B. A., & Thierry, V. (2017). Global and full-depth ocean temperature trends during the early twenty-first century from argo and repeat hydrography. *Journal of Climate*, *30*(6), 1985–1997. https://doi.org/10.1175/JCLI-D-16-0396.1

Duennebier, F. K. (1968). *Spectral variation of the T phase (Tech. Rep.)*. Hawaii Institute of Geophysics.

Duennebier, F. K., & Johnson, R. H. (1967). *T-phase sources and earthquake epicenters in the Pacific basin (Tech. Rep.)*. Hawaii Institute of Geophysics.

Dushaw, B. D., Gaillard, F., & Terre, T. (2017). Acoustic tomography in the canary basin: Meddies and tides. *Journal of Geophysical Research: Oceans*, *122*(11), 8983–9003. https://doi.org/10.1002/2017JC013356

Dziak, R. P., Bohnenstiehl, D. R., & Smith, D. K. (2012). Hydroacoustic monitoring of oceanic spreading centers: Past, present, and future. *Oceanography*, *25*(1), 116–127. https://doi.org/10.5670/oceanog.2012.10

Dziak, R. P., Hammond, S. R., & Fox, C. G. (2011). A 20-year hydroacoustic time series of seismic and volcanic events in the northeast Pacific ocean. *Oceanography*, *24*(3), 280–293. https://doi.org/10.5670/oceanog.2011.79

Elfouhaily, T., Chapron, B., Katsaros, K., & Vandemark, D. (1997). A unified directional spectrum for long and short wind-driven waves. *Journal of Geophysical Research*, *102*(C7), 15781–15796. https://doi.org/10.1029/97JC00467

Forget, G., Campin, J.-M., Heimbach, P., Hill, C. N., Ponte, R. M., & Wunsch, C. (2015). ECCO version 4: An integrated framework for non-linear inverse modeling and global ocean state estimation. *Geoscientific Model Development*, *8*(10), 3071–3104. https://doi.org/10.5194/gmd-8-3071-2015

Fox, C. G., Dziak, R. P., Matsumoto, H., & Schreiner, A. E. (1994). Potential for monitoring low-level seismicity on the Juan-de-Fuca ridge using military hydrophone arrays. *Marine Technology Society Journal*, *27*(4), 22–30.

Fox, C. G., Matsumoto, H., & Lau, T.-K. A. (2001). Monitoring Pacific Ocean seismicity from an autonomous hydrophone array. *Journal of Geophysical Research*, *106*(B3), 4183–4206. https://doi.org/10.1029/2000JB900404

Fung, A., & Lee, K. (1982). A semi-empirical sea-spectrum model for scattering coefficient estimation. *IEEE Journal of Oceanic Engineering*, *7*(4), 166–176. https://doi.org/10.1109/JOE.1982.1145535

Gao, D., Kao, H., & Wang, B. (2021). Misconception of waveform similarity in the identification of repeating earthquakes. *Geophysical Research Letters*, *48*(13), e2021GL092815. https://doi.org/10.1029/2021GL092815

Garrett, C., & Munk, W. (1972). Space-Time scales of internal waves. *Geophysical Fluid Dynamics*, *3*(3), 225–264. https://doi.org/10.1080/03091927208236082

Garrett, C., & Munk, W. (1975). Space-time scales of internal waves: A progress report. *Journal of Geophysical Research (1896-1977)*, *80*(3), 291–297. https://doi.org/10.1029/JC080i003p00291

Godin, O. A. (2021). Contributions of gravity waves in the ocean to T-phase excitation by earthquakes. *Journal of the Acoustical Society of America*, *150*(5), 3999–4017. https://doi.org/10.1121/10.0007283

Hamilton, E. L. (1976). Variations of density and porosity with depth in deep-sea sediments. *Journal of Sedimentary Research*, *46*(2), 280–300. https://doi.org/10.1306/212F6F3C-2B24-11D7-8648000102C1865D

Hamilton, E. L. (1979). Vp/Vs and Poisson's ratios in marine sediments and rocks. *Journal of the Acoustical Society of America*, *66*(4), 1093–1101. https://doi.org/10.1121/1.383344

Hanson, J. A., & Bowman, J. R. (2006). Methods for monitoring hydroacoustic events using direct and reflected T waves in the Indian Ocean. *Journal of Geophysical Research*, *111*(B2). https://doi.org/10.1029/2004JB003609

Harmon, N., Rychert, C., Agius, M., Tharimena, S., Le Bas, T., Kendall, J. M., & Constable, S. (2018). Marine geophysical investigation of the chain fracture zone in the equatorial Atlantic from the PI-LAB experiment. *Journal of Geophysical Research: Solid Earth*, *123*(12), 11016–11030. https://doi.org/10.1029/2018JB015982

Hasselmann, D. E., Dunckel, M., & Ewing, J. A. (1980). Directional wave spectra observed during JONSWAP 1973. *Journal of Physical Oceanography*, *10*(8), 1264–1280. https://doi.org/10.1175/1520-0485(1980)010<1264:DWSODJ>2.0.CO;2

Heezen, B. C., Bunce, E. T., Hersey, J. B., & Tharp, M. (1964). Chain and romanche fracture zones. *Deep-Sea Research and Oceanographic Abstracts*, *11*(1), 11–33. https://doi.org/10.1016/0011-7471(64)91079-4

Hersbach, H., Bell, B., Berrisford, P., Hirahara, S., Horányi, A., Muñoz-Sabater, J., et al. (2020). The ERA5 global reanalysis. *Quarterly Journal of the Royal Meteorological Society*, *146*(730), 1999–2049. https://doi.org/10.1002/qj.3803

Hess, H. (1955). The oceanic crust. *Journal of Marine Research*, *14*(4), 423–439.

Hicks, S. P., Okuwaki, R., Steinberg, A., Rychert, C. A., Harmon, N., Abercrombie, R. E., et al. (2020). Back-propagating supershear rupture in the 2016 Mw 7.1 Romanche transform fault earthquake. *Nature Geoscience*, *13*(9), 647–653. https://doi.org/10.1038/s41561-020-0619-9

Holthuijsen, L. H. (2010). *Waves in oceanic and coastal waters*. Cambridge university press.

Jamet, G., Guennou, C., Guillon, L., Mazoyer, C., & Royer, J.-Y. (2013). T-Wave generation and propagation: A comparison between data and spectral element modeling. *Journal of the Acoustical Society of America*, *134*(4), 3376–3385. https://doi.org/10.1121/1.4818902

Johnson, R. H., Norris, R. A., & Duennebier, F. K. (1968). Abyssally generated T-phases. In L. Knopoff, C. L. Drake, & P. J. Ehart (Eds.), *The crust and upper mantle of the Pacific area, geophysical monograph series* (Vol. 12, pp. 70–78). American Geophysical Union. https://doi.org/10.1029/gm012p0070

Johnson, R. H., Northrop, J., & Eppley, R. (1963). Sources of Pacific T phases. *Journal of Geophysical Research (1896-1977)*, *68*(14), 4251–4260. https://doi.org/10.1029/JZ068i014p04251

Keenan, R. E., & Merriam, L. R. L. (1991). Arctic abyssal T phases: Coupling seismic energy to the ocean sound channel via under-ice scattering. *Journal of the Acoustical Society of America*, *89*(3), 1128–1133. https://doi.org/10.1121/1.400648

Komatitsch, D., & Tromp, J. (1999). Introduction to the spectral element method for three-dimensional seismic wave propagation. *Geophysical Journal International*, *139*(3), 806–822. https://doi.org/10.1046/j.1365-246x.1999.00967.x

Komatitsch, D., & Vilotte, J.-P. (1998). The spectral element method: An efficient tool to simulate the seismic response of 2D and 3D geological structures. *Bulletin of the Seismological Society of America*, *88*(2), 368–392. https://doi.org/10.1785/BSSA0880020368

Krogstad, H. E., & Barstow, S. F. (1999). Directional distributions in ocean wave spectra. In *The ninth international Ocean and polar engineering conference* (Vol. 3, pp. 79–86). Brest, France.

Kuna, V. M., Nábělek, J. L., & Braunmiller, J. (2019). Mode of slip and crust–mantle interaction at oceanic transform faults. *Nature Geoscience*, *12*(2), 138–142. https://doi.org/10.1038/s41561-018-0287-1

Lecoulant, J., Guennou, C., Guillon, L., & Royer, J.-Y. (2019). Three-dimensional modeling of earthquake generated acoustic waves in the ocean in simplified configurations. *Journal of the Acoustical Society of America*, *146*(3), 2113–2123. https://doi.org/10.1121/1.5126009

Lecoulant, J., Oliveira, T. C. A., & Lin, Y.-T. (2021). Three-dimensional modeling of T-wave generation and propagation from a South Mid-Atlantic Ridge earthquake. *Journal of the Acoustical Society of America*, *150*(5), 3807–3824. https://doi.org/10.1121/10.0007072

Leptokaropoulos, K., Rychert, C. A., Harmon, N., & Kendall, J. M. (2023). Seismicity properties of the chain transform fault inferred using data from the PI-LAB experiment. *Journal of Geophysical Research: Solid Earth*, *128*(3), e2022JB024804. https://doi.org/10.1029/2022JB024804

Levine, M. D. (2002). A modification of the Garrett–Munk internal wave spectrum. *Journal of Physical Oceanography*, *32*(11), 3166–3181. https://doi.org/10.1175/1520-0485(2002)032<3166:AMOTGM>2.0.CO;2

Li, Z., Shen, Z., Yang, Y., Williams, E., Wang, X., & Zhan, Z. (2021). Rapid response to the 2019 ridgecrest earthquake with distributed acoustic sensing. *AGU Advances*, *2*(2), e2021AV000395. https://doi.org/10.1029/2021AV000395

Lin, C.-W., Chuang, L. Y.-L., Huang, C.-F., Chen, C.-W., & Kuo, B.-Y. (2014). T-wave observations on ocean-bottom seismometers offshore eastern Taiwan. In *Oceans 2014 - TAIPEI* (pp. 1–5). https://doi.org/10.1109/OCEANS-TAIPEI.2014.6964430

Linehan, D. (1940). Earthquakes in the west Indian region. *Eos, Transactions American Geophysical Union*, *21*(2), 229–232. https://doi.org/10.1029/TR021i002p00229

Longuet-Higgins, M. S., Cartwright, D. E., & Smith, N. D. (1963). Observation of the directional spectrum of sea waves using the motions of a floating buoy. In *Ocean wave spectra* (pp. 111–136). Prentice-Hall Inc.

McDougall, T. J., & Barker, P. M. (2011). Getting started with TEOS-10 and the Gibbs Seawater (GSW) oceanographic toolbox. *Scor/Iapso WG*, *127*(532), 1–28.

Munk, W. (1980). Internal wave spectra at the buoyant and inertial frequencies. *Journal of Physical Oceanography*, *10*(11), 1718–1728. https://doi.org/10.1175/1520-0485(1980)010<1718:IWSATB>2.0.CO;2

Munk, W. (1981). Internal waves and small-scale processes. *Evolution of Physical Oceanography*.

Niwa, Y., & Hibiya, T. (2001). Numerical study of the spatial distribution of the M2 internal tide in the Pacific Ocean. *Journal of Geophysical Research*, *106*(C10), 22441–22449. https://doi.org/10.1029/2000JC000770

Norris, R. A., & Johnson, R. H. (1969). Submarine volcanic eruptions recently located in the Pacific by Sofar Hydrophones. *Journal of Geophysical Research (1896-1977)*, *74*(2), 650–664. https://doi.org/10.1029/JB074i002p00650

Ocean Networks Canada. (2009). NEPTUNE seismic stations [Dataset]. *International Federation of Digital Seismograph Networks*. https://doi.org/10.7914/SN/NV

Okal, E. A. (2008). The generation of T waves by earthquakes. *Advances in Geophysics*, *49*, 1–65. https://doi.org/10.1016/S0065-2687(07)49001-X

Olive, J.-A., & Escartín, J. (2016). Dependence of seismic coupling on normal fault style along the Northern Mid-Atlantic Ridge. *Geochemistry, Geophysics, Geosystems*, *17*(10), 4128–4152. https://doi.org/10.1002/2016GC006460

Oliveira, T. C. A., & Lin, Y.-T. (2019). Three-dimensional global scale underwater sound modeling: The T-phase wave propagation of a Southern Mid-Atlantic Ridge earthquake. *Journal of the Acoustical Society of America*, *146*(3), 2124–2135. https://doi.org/10.1121/1.5126010

Pan, J., & Dziewonski, A. M. (2005). Comparison of mid-oceanic earthquake epicentral differences of travel time, centroid locations, and those determined by autonomous underwater hydrophone arrays. *Journal of Geophysical Research*, *110*(B7). https://doi.org/10.1029/2003JB002785

Park, M., Odom, R. I., & Soukup, D. J. (2001). Modal scattering: A key to understanding oceanic T-waves. *Geophysical Research Letters*, *28*(17), 3401–3404. https://doi.org/10.1029/2001GL013472

Parnell-Turner, R., Smith, D. K., & Dziak, R. P. (2022). Hydroacoustic monitoring of seafloor spreading and transform faulting in the equatorial Atlantic ocean. *Journal of Geophysical Research: Solid Earth*, *127*(7), e2022JB024008. https://doi.org/10.1029/2022JB024008

Peng, S., Callies, J., Wu, W., & Zhan, Z. (2024). Seismic Ocean thermometry of the Kuroshio extension region. *Journal of Geophysical Research: Oceans*, *129*(2), e2023JC020636. https://doi.org/10.1029/2023JC020636

Pierson, W. J., & Moskowitz, L. (1964). A proposed spectral form for fully developed wind seas based on the similarity theory of S. A. Kitaigorodskii. *Journal of Geophysical Research (1896-1977)*, *69*(24), 5181–5190. https://doi.org/10.1029/JZ069i024p05181

Pierson, W. J., Neuman, G., & James, R. W. (1955). Practical methods for observing and forecasting ocean waves by means of wave spectra and statistics. *Reprinted 1971)*. https://doi.org/10.25607/OBP-985

Polzin, K. L., & Lvov, Y. V. (2011). Toward regional characterizations of the oceanic internal wavefield. *Reviews of Geophysics*, *49*(4). https://doi.org/10.1029/2010RG000329

Purkey, S. G., & Johnson, G. C. (2010). Warming of global abyssal and deep Southern Ocean waters between the 1990s and 2000s: Contributions to global heat and sea level rise budgets. *Journal of Climate*, *23*(23), 6336–6351. https://doi.org/10.1175/2010JCLI3682.1

Romeiser, R., Alpers, W., & Wismann, V. (1997). An improved composite surface model for the radar backscattering cross section of the ocean surface: 1. Theory of the model and optimization/validation by scatterometer data. *Journal of Geophysical Research*, *102*(C11), 25237–25250. https://doi.org/10.1029/97JC00190

Ryan, W. B. F., Carbotte, S. M., Coplan, J. O., O'Hara, S., Melkonian, A., Arko, R., et al. (2009). Global multi-resolution Topography synthesis. *Geochemistry, Geophysics, Geosystems*, *10*(3). https://doi.org/10.1029/2008GC002332

Sandwell, D. T., Harper, H., Tozer, B., & Smith, W. H. F. (2021). Gravity field recovery from geodetic altimeter missions. *Advances in Space Research*, *68*(2), 1059–1072. https://doi.org/10.1016/j.asr.2019.09.011

Sato, H., Fehler, M. C., & Maeda, T. (2012). *Seismic wave propagation and scattering in the heterogeneous earth*. Springer Science and Business Media.

Schlaphorst, D., Rychert, C. A., Harmon, N., Hicks, S. P., Bogiatzis, P., Kendall, J.-M., & Abercrombie, R. E. (2023). Local seismicity around the chain transform fault at the Mid-Atlantic Ridge from OBS observations. *Geophysical Journal International*, *234*(2), 1111–1124. https://doi.org/10.1093/gji/ggad124

Semedo, A., Sušelj, K., Rutgersson, A., & Sterl, A. (2011). A global view on the wind sea and swell climate and variability from ERA-40. *Journal of Climate*, *24*(5), 1461–1479. https://doi.org/10.1175/2010JCLI3718.1

Shen, Z. (2024). High-resolution chain transform fault bathymetry from the PI-LAB experiment [Dataset]. *Zenodo*. https://doi.org/10.5281/zenodo.13543715

Shen, Z., & Wu, W. (2024). Ocean bottom distributed acoustic sensing for Oceanic seismicity detection and seismic Ocean thermometry. *Journal of Geophysical Research: Solid Earth*, *129*(3), e2023JB027799. https://doi.org/10.1029/2023JB027799

Slack, P. D., Fox, C. G., & Dziak, R. P. (1999). P wave detection thresholds, Pn velocity estimates, and T wave location uncertainty from oceanic hydrophones. *Journal of Geophysical Research*, *104*(B6), 13061–13072. https://doi.org/10.1029/1999JB900112

Smith, D. K., Tolstoy, M., Fox, C. G., Bohnenstiehl, D. R., Matsumoto, H., & J. Fowler, M. (2002). Hydroacoustic monitoring of seismicity at the slow-spreading Mid-Atlantic Ridge. *Geophysical Research Letters*, *29*(11), 13–14. https://doi.org/10.1029/2001GL013912

Straume, E. O., Gaina, C., Medvedev, S., Hochmuth, K., Gohl, K., Whittaker, J. M., et al. (2019). GlobSed: Updated total sediment thickness in the world's oceans. *Geochemistry, Geophysics, Geosystems*, *20*(4), 1756–1772. https://doi.org/10.1029/2018GC008115

Sugioka, H., Fukao, Y., & Hibiya, T. (2005). Submarine volcanic activity, ocean-acoustic waves and internal ocean tides. *Geophysical Research Letters*, *32*(24). https://doi.org/10.1029/2005GL024001

Sykes, L. R. (1967). Mechanism of earthquakes and nature of faulting on the mid-oceanic ridges. *Journal of Geophysical Research*, *72*(8), 2131–2153. https://doi.org/10.1029/JZ072i008p02131

Tepp, G., & Dziak, R. P. (2021). The seismo-acoustics of submarine volcanic eruptions. *Journal of Geophysical Research: Solid Earth*, *126*(4), e2020JB020912. https://doi.org/10.1029/2020JB020912

Tolstoy, I., & Ewing, M. (1950). The T phase of shallow-focus earthquakes. *Bulletin of the Seismological Society of America*, *40*(1), 25–51. https://doi.org/10.1785/BSSA0400010025

Torsethaugen, K., & Haver, S. (2004). Simplified double peak spectral model for ocean waves. In *The fourteenth international Ocean and polar engineering conference. Toulon, France*.

Tozer, B., Sandwell, D. T., Smith, W. H. F., Olson, C., Beale, J. R., & Wessel, P. (2019). Global bathymetry and Topography at 15 Arc Sec: SRTM15+. *Earth and Space Science*, *6*(10), 1847–1864. https://doi.org/10.1029/2019EA000658

Van Uffelen, L. J., Worcester, P. F., Dzieciuch, M. A., & Rudnick, D. L. (2009). The vertical structure of shadow-zone arrivals at long range in the ocean. *Journal of the Acoustical Society of America*, *125*(6), 3569–3588. https://doi.org/10.1121/1.3117430

Various Institutions. (1965). International miscellaneous stations [Dataset]. *International Federation of Digital Seismograph Networks*. https://doi.org/10.7914/VEFQ-VH75

von Schuckmann, K., Gaillard, F., & Le Traon, P.-Y. (2009). Global hydrographic variability patterns during 2003–2008. *Journal of Geophysical Research*, *114*(C9). https://doi.org/10.1029/2008JC005237

Wech, A., Tepp, G., Lyons, J., & Haney, M. (2018). Using earthquakes, T waves, and infrasound to investigate the eruption of Bogoslof Volcano, Alaska. *Geophysical Research Letters*, *45*(14), 6918–6925. https://doi.org/10.1029/2018GL078457

Williams, C. M., Stephen, R. A., & Smith, D. K. (2006). Hydroacoustic events located at the intersection of the Atlantis (30°N) and Kane (23° 40′N) transform faults with the Mid-Atlantic Ridge. *Geochemistry, Geophysics, Geosystems*, *7*(6). https://doi.org/10.1029/2005GC001127

Williams, K. L., Henyey, F. S., Rouseff, D., Reynolds, S. A., & Ewart, T. E. (2001). Internal wave effects on high-frequency acoustic propagation to horizontal arrays-experiment and implications to imaging. *IEEE Journal of Oceanic Engineering*, *26*(1), 102–112. https://doi.org/10.1109/48.917939

Wu, W., Shen, Z., Peng, S., Zhan, Z., & Callies, J. (2023). Seismic Ocean thermometry using CTBTO hydrophones. *Journal of Geophysical Research: Solid Earth*, *128*(9), e2023JB026687. https://doi.org/10.1029/2023JB026687

Wu, W., Zhan, Z., Peng, S., Ni, S., & Callies, J. (2020). Seismic ocean thermometry. *Science*, *369*(6510), 1510–1515. https://doi.org/10.1126/science.abb9519

Yang, Y., & Forsyth, D. W. (2003). Improving epicentral and magnitude estimation of earthquakes from T phases by considering the excitation function. *Bulletin of the Seismological Society of America*, *93*(5), 2106–2122. https://doi.org/10.1785/0120020215

Yu, Z., Singh, S. C., Gregory, E. P. M., Maia, M., Wang, Z., & Brunelli, D. (2021). Semibrittle seismic deformation in high-temperature mantle mylonite shear zone along the Romanche transform fault. *Science Advances*, *7*(15), eabf3388. https://doi.org/10.1126/sciadv.abf3388

Yun, S., Lee, W. S., Dziak, R. P., & Matsumoto, H. (2022). Numerical study on the characteristics of abyssal T-wave envelopes controlled by earthquake source parameters. *Seismological Research Letters*, *93*(4), 2189–2200. https://doi.org/10.1785/0220210264

Zang, C., Wu, W., Ni, S., & Xu, M. (2024). A reciprocity-based efficient method for improved source parameter estimation of submarine earthquakes with hybrid 3-D teleseismic green's functions. *Journal of Geophysical Research: Solid Earth*, *129*(5), e2023JB028174. https://doi.org/10.1029/2023JB028174